

## Article

# Effect of Viscosity Action and Capillarity on Pore-Scale Oil–Water Flowing Behaviors in a Low-Permeability Sandstone Waterflood

Tao Ning <sup>1</sup>, Meng Xi <sup>1</sup>, Bingtao Hu <sup>2</sup> , Le Wang <sup>3</sup>, Chuanqing Huang <sup>4</sup> and Junwei Su <sup>2,\*</sup> 

<sup>1</sup> The Management Headquarters of Water Injection Project, Yanchang Oil Field Co. Ltd., Yan'an 716000, China; ningtao9226@sxyopc.com (T.N.); 18729325132@163.com (M.X.)

<sup>2</sup> School of Human Settlements and Civil Engineering, Xi'an Jiaotong University, Xi'an 710049, China; hubingtao@stu.xjtu.edu.cn

<sup>3</sup> Mechanical Engineering College, Xi'an Shiyou University, Xi'an 710065, China; 180907@xsyu.edu.cn

<sup>4</sup> School of Chemistry and Chemical Engineering, Shaanxi University of Science and Technology, Xi'an 710021, China; huangcq@sust.edu.cn

\* Correspondence: sujunwei@mail.xjtu.edu.cn; Tel.: +86-029-8896-5100

**Abstract:** Water flooding technology is an important measure to enhance oil recovery in oilfields. Understanding the pore-scale flow mechanism in the water flooding process is of great significance for the optimization of water flooding development schemes. Viscous action and capillarity are crucial factors in the determination of the oil recovery rate of water flooding. In this paper, a direct numerical simulation (DNS) method based on a Navier–Stokes equation and a volume of fluid (VOF) method is employed to investigate the dynamic behavior of the oil–water flow in the pore structure of a low-permeability sandstone reservoir in depth, and the influencing mechanism of viscous action and capillarity on the oil–water flow is explored. The results show that the inhomogeneity variation of viscous action resulted from the viscosity difference of oil and water, and the complex pore-scale oil–water two-phase flow dynamic behaviors exhibited by capillarity play a decisive role in determining the spatial sweep region and the final oil recovery rate. The larger the viscosity ratio is, the stronger the dynamic inhomogeneity will be as the displacement process proceeds, and the greater the difference in distribution of the volumetric flow rate in different channels, which will lead to the formation of a growing viscous fingering phenomenon, thus lowering the oil recovery rate. Under the same viscosity ratio, the absolute viscosity of the oil and water will also have an essential impact on the oil recovery rate by adjusting the relative importance between viscous action and capillarity. Capillarity is the direct cause of the rapid change of the flow velocity, the flow path diversion, and the formation of residual oil in the pore space. Furthermore, influenced by the wettability of the channel and the pore structure's characteristics, the pore-scale behaviors of capillary force—including the capillary barrier induced by the abrupt change of pore channel positions, the inhibiting effect of capillary imbibition on the flow of parallel channels, and the blockage effect induced by the newly formed oil–water interface—play a vital role in determining the pore-scale oil–water flow dynamics, and influence the final oil recovery rate of the water flooding.

**Keywords:** water flooding; pore scale; enhanced oil recovery; viscosity; capillarity



**Citation:** Ning, T.; Xi, M.; Hu, B.; Wang, L.; Huang, C.; Su, J. Effect of Viscosity Action and Capillarity on Pore-Scale Oil–Water Flowing Behaviors in a Low-Permeability Sandstone Waterflood. *Energies* **2021**, *14*, 8200. <https://doi.org/10.3390/en14248200>

Academic Editor: Marcin Kremieniewski

Received: 5 October 2021

Accepted: 19 November 2021

Published: 7 December 2021

**Publisher's Note:** MDPI stays neutral with regard to jurisdictional claims in published maps and institutional affiliations.



**Copyright:** © 2021 by the authors. Licensee MDPI, Basel, Switzerland. This article is an open access article distributed under the terms and conditions of the Creative Commons Attribution (CC BY) license (<https://creativecommons.org/licenses/by/4.0/>).

## 1. Introduction

Crude oil, a typical conventional strategical energy resource, plays a significant role in the development of human industrial civilization and economic prosperity. Crude oil is extracted from the production well due to the natural energy and pressure of the reservoirs in the primary oil recovery process. Water flooding technology is widely utilized to further improve the efficiency of oil production, which will ultimately lead to the high ratio of water to oil of producing wells, thus decreasing the oil production efficiency [1]. It is widely acknowledged that ~60% of the original crude oil is still trapped in the reservoirs after

water flooding [2]. The crude oil extraction from oil reservoirs is characterized by a typical multiphase flow in porous media, and the flow conditions, the properties of the injected fluid and the pore structure characteristics have a huge impact on the multiphase flow in porous media. The macroscopic characteristics of the water flooding development of sandstone reservoirs are the comprehensive results of oil–water two-phase flow within a large number of microscopic pore channels. The investigation of the flow dynamic characteristic oil–water two-phase flow within porous media at the pore-scale in depth is of great significance to understand the macroscopic phenomenon of the water flooding development process. The pore-scale investigation of multiphase flow behavior and the dynamic process within reservoir rock contributes to clarify the underlying dynamic mechanisms of certain macroscopic water flooding phenomena [3–7].

In the study of pore-scale flow, the gravity effect is generally relatively small, and can be ignored. In such a situation, viscous action and capillarity are essential factors in affecting the process of immiscible displacements in porous media [8]. The current enhanced oil recovery approaches are adopted to improve the oil recovery rate by adjusting the displacement front through the regulation of the viscous effect or capillary effect. For instance, the polymer flooding technique is employed to enhance the oil recovery rate mainly by increasing the viscosity of the displacement fluid, decreasing the viscosity ratio of oil to water, and increasing the sweep region of the displacement fluid [9]. On the other hand, the surfactant flooding technique is used to mobilize the residual oil trapped by the capillary force in the pore space by reducing the interfacial tension of oil and water through the addition of surfactants to the displacement fluid [10]. The increasing injection rate technique is used to mobilize the residual oil by increasing the relative magnitude of the viscous action and capillary force. Particle flooding techniques are used to increase the resistance of the water bearing channel with polymer particles (increasing the effective viscosity of the flooding agents) to make the fluid divert to the oil-bearing channel, so as to improve the oil recovery [11]. Thus, the investigation of the effect of the viscosity action and capillary on the two-phase flow is essentially important in order to enhance oil recovery.

The effects of viscous action and capillary on two-phase flow in the porous media have been widely studied [12]. In terms of the viscous effect on the flow, Homsy systematically reviewed the viscous fingering in porous media in 1987, and pointed out that the root cause of the viscous fingering formation is due to the viscosity difference of two phases [12–23]. The two-phase displacement process within a two-dimensional porous medium was investigated by Cottin, and the variation process of capillary fingering to viscous fingering was obtained [13]. Tsuji investigated the displacement process in three-porous media under different capillary numbers and viscosity ratios, obtained the displacement diagram of three-dimensional porous media, and analyzed the macroscopic characteristics of different displacement modes [14]. Hu investigated the effect of the interplay between disorder and the contact angle on the pore-scale flow behaviors, and obtained a quasi-static immiscible displacement phase diagram in disordered porous media. [15]. Singh reviewed the capillary-dominated flow behaviors in the porous media [16]. Yang investigated the effect of the wettability and capillarity on the remaining oil distribution in 3D porous media [17]. Guo studied the effect of the viscosity and interfacial tension on the distribution of the residual oil distribution [18]. Influenced by the complexity of the pore structure, the morphology of the oil–water interface will change abruptly during the advancing process, thus causing complex flow behaviors induced by the abrupt change of interfacial tension. Specific pore-scale flow behaviors—including the Haines jumps [19], snap-off effect [20–22] and the capillary barrier [11,23]—have been investigated by many researchers at the infancy stage.

Although extensive investigations of the effects of viscous action and capillarity on the flow have been conducted in previous works, these studies mainly focused on the analysis and characterization of the flow behaviors from the observed phenomena, and there are few studies concerning the underlying dynamic mechanism behind these phenomena or

the effects of certain phenomena (Haines jumps, the snap-off effect or the capillary barrier, for instance) on the immiscible fluid displacement processes in the open literature.

The pore structure characteristics of a low-permeability sandstone reservoir are obviously different from those of medium- and high-permeability sandstone reservoirs. Compared with medium- and high-permeability sandstone, a low-permeability sandstone reservoir has a smaller pore size and a larger pore–throat ratio. The capillary effect plays a more obvious role in the process of pore-scale flow. The pore space of a low-permeability sandstone reservoir has more unique and complex pore-scale flow characteristics (such as the capillary valve effect). Limited by the chip fabrication process and the accuracy of displacement equipment, there are few studies on pore-scale oil–water movement in low-permeability sandstone reservoirs. Pore-scale direct numerical simulation technology is generally an important technology to study low-permeability sandstone reservoirs. In this paper, the water flooding process in low-permeability sandstone oil reservoirs is numerically simulated using the Navier–Stokes equation coupled with the volume of fluid (VOF) method to investigate the effect of viscous action and capillarity on the pore-scale oil–water flow process from the point of view of two-phase dynamics. The dynamic processes of several specific phenomena or events are analyzed, which will deepen the established understanding of water flooding in low-permeability sandstone oil reservoirs. The numerical model of an oil–water two-phase flow is presented first, then an in-depth analysis of the viscous and capillary effects of the two-phase flow process is performed; results and discussions concerning the numerical simulation of the water flooding process in low-permeability sandstone oil reservoirs follow, and finally the conclusions are drawn in the final part.

## 2. Dynamic Model and Solution Algorithm for Oil–Water Two-Phase Pore-Scale Flow

The macroscopic characteristics exhibited in the water flooding process of sandstone reservoirs are a concentrated reflection of microscopic oil–water flow in a large number of pore channels. An in-depth investigation on the dynamic process of oil–water two-phase flow in the pore space, as well as the relevant oil–water two-phase flow characteristics, is of great significance for the clarification of the underlying dynamic mechanisms of the water flooding process. In this section, the dynamic equations describing the oil–water two-phase flow in the pore space are presented firstly, followed by its solution algorithm.

In this paper, Navier–Stokes equations are used to describe the oil–water two-phase flow in an Eulerian framework, the VOF (Volume of Fluid) method is used to track the spatial distribution of the oil and water, and the contact angle is employed for the characterization of the wettability of the reservoir rock [24].

### 2.1. Pore-Scale Dynamic Model for Oil–Water Movement in Porous Media

#### 2.1.1. Mass Conservation Equation

The differential form of the mass equation for an incompressible oil–water two-phase flow is given by

$$\nabla \cdot \mathbf{u} = 0, \quad (1)$$

where  $\mathbf{u}$  is average velocity of the oil phase and water phase,  $\text{m} \cdot \text{s}^{-1}$ .

#### 2.1.2. Momentum Conservation Equation

The differential form of the momentum conservation equation for the oil–water two-phase flow is given by

$$\frac{\partial \rho \mathbf{u}}{\partial t} + \nabla \cdot (\rho \mathbf{u} \mathbf{u}) - \nabla \cdot (\mu \boldsymbol{\tau}) = -\nabla p + \rho \mathbf{g} + \mathbf{F}_\sigma, \quad (2)$$

where  $\rho$  is average density of the oil phase and water phase,  $\text{kg} \cdot \text{m}^{-3}$ ;  $\mu$  is average dynamic viscosity of the two phases,  $\text{Pa} \cdot \text{s}$ ;  $p$  is dynamic pressure,  $\text{Pa}$ ;  $\mathbf{g}$  is acceleration of gravity,

$\text{m}\cdot\text{s}^{-2}$ ;  $\mathbf{F}_\sigma$  is the interfacial tension (IFT) between oil and water,  $\text{kg}\cdot\text{m}^{-2}\cdot\text{s}^{-2}$ ; and  $\boldsymbol{\tau}$  is the rate of strain tensor,  $\text{s}^{-1}$ , which is given as follows:

$$\boldsymbol{\tau} = (\nabla\mathbf{u} + (\nabla\mathbf{u})^T), \quad (3)$$

### 2.1.3. Oil–Water Interfacial Tension

The last term,  $\mathbf{F}_\sigma$ , which appeared on the right-hand side of Equation (1) represents the interfacial tension between oil and water, which can be expressed as follows:

$$\mathbf{F}_\sigma = \sigma\delta_s k \mathbf{n}, \quad (4)$$

where  $\sigma$  is the surface tension coefficient,  $\text{N}\cdot\text{m}^{-1}$ ;  $\delta_s$  is the area of the oil–water interface per unit volume,  $\text{m}^{-1}$ ;  $k$  is the curvature of the oil–water interface,  $\text{m}^{-1}$ ; and  $\mathbf{n}$  is the unit-normal vector of the interface.

The area of the oil–water interface per unit volume  $\delta_s$  is given by

$$\delta_s = |\nabla\alpha|, \quad (5)$$

where  $\alpha$  is the volume fraction of the water phase.

The unit-normal vector of the interface  $\mathbf{n}$  is given by

$$\mathbf{n} = \frac{\nabla\alpha}{|\nabla\alpha|}, \quad (6)$$

The curvature of the oil–water interface  $k$  is given by

$$k = \nabla\cdot\mathbf{n}, \quad (7)$$

It should be stressed that the interfacial tension given in Equation (4) is a force on the oil–water interface with an area of  $\delta_s$ . It is different from the capillary force in a tube, which is the total force of the interaction action. It is also different from the capillary pressure function for the porous media. The macroscopic capillary pressure function of the porous media is the result of the interface tension in the microscopic view. According to whether the interface moves or not, the macro impact of the interfacial tension can be divided into two parts: the moving part is described by the macro capillary pressure function (because the capillary force is directly related to the two-phase velocity described in the black oil model for the macroscopic description of the oil–water flow in the porous media). The binding effect of the interfacial tension on oil causes the oil not to move, which is usually described by the endpoint of the relative permeability curve in the macroscopic model. With the model given in Equation (4), the effect of the interface tension of the static oil–water interface (such as the capillary valve effect) and the dynamic oil–water interface (such as the osmotic effect and the capillary inhibition effect) on the pore-scale oil–water motion is taken into account.

### 2.1.4. Oil–Water Volume Fraction

The VOF method is used to track the spatial distribution of the oil–water two-phase flow. The interface is determined by solving the equation for the volume fraction of water phase  $\alpha$  in each cell. When the value of  $\alpha$  is unity, the cell is fully occupied by the water phase; when the value of  $\alpha$  is zero, the cell is fully occupied by the oil phase; when the value of  $\alpha$  is in the range of 0 to 1, the cell contains the free interface. The equation for the volume fraction of the water phase is expressed as follows:

$$\frac{\partial\alpha}{\partial t} + \nabla\cdot(\alpha\mathbf{u}) = 0, \quad (8)$$

With Equation (8), the distribution of water and oil in the pore space can be obtained. The homogeneity of the two-phase flow caused by pore-scale flow behaviors (emulsification or snap-off, for instance) can be obtained easily.

### 2.1.5. Wettability

The contact angle is commonly employed to characterize the wettability of the reservoir rock. The wettability of the pore wall can be classified into three regimes based on different water contact angles: hydrophilicity (water-wet), intermediate-wettability, and hydrophobicity (oil-wet). The wettability of the pore walls is of great importance in order to accurately simulate the oil–water two-phase flow and predict the distribution of the residual oil. The contact angle of the rock is affected by the surface roughness, the composition of the rock, and the thickness of the water film. It is difficult to accurately determine the contact angle of realistic reservoir rock considering the mixed wettability and the variation of the contact angle with spatial locations. The wettability regimes of water-wettability, intermediate-wettability and oil-wettability are considered by adjusting the value of the contact angle in this paper.

In order to model the wettability of the rock, the contact angle is imposed as a boundary condition, as illustrated in Figure 1. The unit vector normal to the interface needs to be modified as the following from

$$\mathbf{n} = \mathbf{n}_w \cos \theta + \mathbf{s}_w \sin \theta, \quad (9)$$

where  $\mathbf{n}_w$  is the unit vector normal to the wall;  $\mathbf{s}_w$  is the unit vector perpendicular to the contact line, tangential to and pointing into the wetting–solid interface surface; and  $\theta$  is the contact angle, radian.

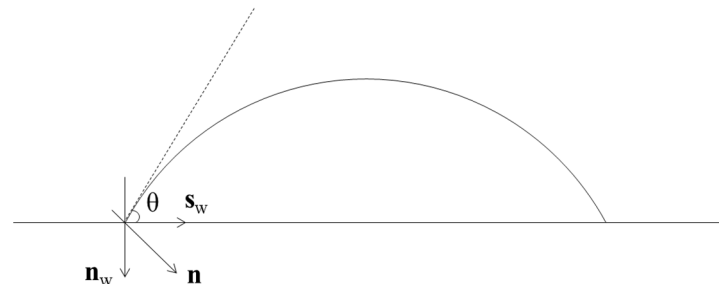


**Figure 1.** Illustration of the implementation of the contact angle boundary condition.

### 2.1.6. Averaging Properties of the Oil–Water Flow

In Equation (2),  $\rho$  and  $\mu$  represent the average density and dynamic viscosity of the water phase and the oil phase, respectively, which can be calculated respectively by Equations (10) and (11):

$$\rho = \alpha \rho_w + (1 - \alpha) \rho_o, \quad (10)$$

$$\mu = \alpha \mu_w + (1 - \alpha) \mu_o, \quad (11)$$

where  $\rho_w$  is the density of the water phase,  $\text{kg}\cdot\text{m}^{-3}$ ;  $\rho_o$  is the density of the oil phase,  $\text{kg}\cdot\text{m}^{-3}$ ;  $\mu_w$  is the dynamic viscosity of the water phase,  $\text{Pa}\cdot\text{s}$ ; and  $\mu_o$  is the dynamic viscosity of the oil phase,  $\text{Pa}\cdot\text{s}$ .

## 2.2. Solution Method and Procedure

### 2.2.1. Solution Method

The PISO (Pressure-Implicit with Splitting of Operators) algorithm is used to decouple the continuity and momentum equation [25]. In order to separate the pressure difference caused by surface tension from the actual pressure, Equation (2) can be written as

$$a_p \mathbf{u} = A_H - \nabla p_d - \nabla p_c \quad (12)$$

where  $a_p$  is the diagonal coefficient in coefficient matrix discretized from Equation (2).  $p_c$  is the pressure gradient caused by surface tension, and  $A_H$  can be written as

$$A_H = \sum_N a_N \mathbf{u} + b \quad (13)$$

where  $a_N$  is the implicit contribution coefficient of neighbor cells to the cell concerned, and  $b$  includes all of the explicit discretization contributions except pressure.

Both sides of Equation (13) are divided by  $a_p$ , and we obtain a new equation as follows:

$$\mathbf{u} = \frac{A_H}{a_p} - \frac{\nabla p_d}{a_p} - \frac{\nabla p_c}{a_p} \quad (14)$$

Equation (14) should satisfy the continuity Equation (1). As such, Equation (14) also can be transformed to the following form:

$$\nabla \cdot \left( \frac{1}{a_p} \nabla p_d \right) = \nabla \cdot \left( \frac{A_H}{a_p} \right) - \nabla \cdot \left( \frac{1}{a_p} \nabla p_c \right) \quad (15)$$

Equation (15) is the pressure equation derived from the PISO algorithm. Solving the equation can obtain a new pressure and substitute it into Equation (14) to update the velocity. The finite volume method based on a collocated grid is used in the discretization process in this paper. While updating the body-center velocity, it is necessary to update the flow rate on the interface of the element in order to discretize the convection term next time. The surface flow rate is updated using the interpolation on the surface of Equation (14):

$$\varphi_f = \nabla \cdot \left( \frac{A_H}{a_p} \right)_f S_f - \left( \frac{\nabla p_d}{a_p} \right)_f S_f - \left( \frac{\nabla p_c}{a_p} \right)_f S_f \quad (16)$$

It should be noted that it is necessary to calculate the pressure gradient caused by the surface tension when updating the unit interface flow rate by solving Equation (15) or Equation (16).

### 2.2.2. Solution Procedure

The arbitrary polyhedral finite volume method in OpenFOAM [26,27] is used to discretize the pore-scale dynamic equations. The following procedure is used to solve the pore-scale models:

- Step 1: Solve the momentum conservation equation (Equation (2)) to predict the velocity.
- Step 2: Solve the pressure equation (Equation (15)) with the velocity predicted in Step 1.
- Step 3: Correct the volume flux at the cell faces using Equation (16) and the velocity at the cell centers using Equation (14), respectively.
- Step 4: Repeat Step 2 and Step 3 until the convergence of pressure and velocity.
- Step 5: Solve the water phase volume fraction (Equation (8)).
- Step 6: Calculate the oil–water interfacial force using Equation (4).
- Step 7: Update the average density and average viscosity using Equations (10) and (11).
- Step 8: Go to Step 1 for the next time step.

With Steps 1–8 we can obtain the pore-scale distribution of the pressure, velocity, oil fraction, water fraction. A more elaborate description of the solution techniques and model validation can be found in our previous work [6].

### 3. Viscous Force and Capillary Force in a Capillary Tube

From the dynamic equation of the oil–water two-phase flow (Equation (2)), it can be seen that the oil–water two-phase flow within the pore space is influenced by factors including the applied pressure difference, the viscous effect, the interfacial effect and the gravity effect. The relative magnitudes of the various effects affect the flow behavior of the oil–water two-phase flow within the pore space, and ultimately determine the oil

recovery rate of the water flooding method. In general, the water flooding process is a horizontal displacement, and the following section only focuses on the viscous effect and interfacial effect.

### 3.1. Viscous Force

Oil and water are viscous fluids, and the oil–water two-phase flow within the pore space of the sandstone reservoir is subject to the viscous force. Most of the energy in the process of oil recovery by water flooding is consumed by the viscous effect [28]. The strength of the two-phase viscous effect can be described by the viscous force. Figure 2 demonstrates the oil and water distribution in a capillary tube; the radius of the capillary tube is  $R$ , the length of the water side is  $L_1$ , the length of the oil side is  $L_2$ , and the velocity of the flow is  $u$ . According to the Hagen–Poiseuille formula, the viscous force of the fluid can be expressed as

$$F_{vis} = \frac{8(\mu_w L_1 + \mu_o L_2)u}{R^2}, \quad (17)$$

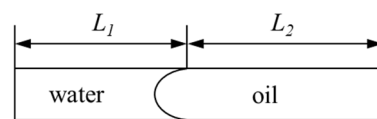


**Figure 2.** Schematic diagram of the oil and water distribution in a capillary tube.

Equation (17) can be further written in the following form:

$$F_{vis} = \frac{8(\mu_w \alpha_w + \mu_o (1 - \alpha_w))Lu}{R^2}, \quad (18)$$

where  $L$  is the length of the capillary tube, and is defined as the sum of  $L_1$  and  $L_2$ .

It can be seen from Equation (17) or Equation (18) that the viscous force increases with the increase of the flow rate and the decrease of the capillary tube radius, while the viscous force decreases with the increase of the water content (the viscosity of water is generally lower than that of oil).

It can be concluded from Equation (18) that, with the displacement, the oil in the capillary is gradually replaced by water, and the viscous resistance of the capillary decreases gradually. If the oil–water viscosity ratio is 5, the water in the capillary changes from oil to water, and the resistance becomes 0.2 times that of the original. In the actual water flooding process, with the same pore structure characteristics, the flow resistance in the water-bearing area is 0.2 times that in the oil-bearing area. This inhomogeneity is caused by fluid phase distribution, which is called dynamic inhomogeneity in this paper.

Equation (18) can be further written as the following form:

$$F_{vis} = \frac{8(\mu_w \alpha_w + \mu_o (1 - \alpha_w))LQ}{\pi R^4}, \quad (19)$$

where  $Q$  is the volumetric flow rate of the capillary tube,  $\text{m}^3 \cdot \text{s}^{-1}$ .

It can be concluded from Equation (19) that the viscous resistance increases 10,000 times when the capillary radius is reduced by a factor of 10 under the same injection rate and the same water content of the capillary tube. The injection pressure of a low-permeability sandstone reservoir is much higher than that of the high-permeability sandstone reservoir under the same injection flow rate.

### 3.2. Capillary Force

Because the oil and water phases are immiscible, there is an interface between the oil and water phases in the process of flowing in the pore channel. Because the molecular forces on both sides of the interface are not equal, an additional effect is exerted on the flow of oil and water by the interface. The magnitude of the additional force can be expressed by the interfacial tension. Figure 2 shows the capillary force in a straight pipe (the resultant

force of local interfacial tension), which can be expressed as

$$p_c = \frac{\sigma \cos(\theta)}{R}, \quad (20)$$

The following conclusions can be drawn from Equation (20):

- (1) When  $\theta < 90^\circ$ , the wettability is water-wet, the pressure difference  $\Delta p > 0$ , the capillary force is a type of driving force, and the direction is consistent with the direction of the oil–water flow.
- (2) When  $\theta = 90^\circ$ , the wettability is intermediate-wet, the pressure difference  $\Delta p = 0$ , and the value of the capillary force is zero.
- (3) When  $\theta > 90^\circ$ , the wettability is oil-wet, the pressure difference  $\Delta p < 0$ , the direction of the capillary force is opposite to the direction of the water flooding, and the capillary force is a type of resistance.
- (4) The magnitude of the capillary force is inversely proportional to the radius of the capillary tube: the smaller the radius, the larger the capillary force.

The pore radii at the different locations of the pore channels in real sandstone are different, and there are pores and throats. There are abrupt changes of the pore radius at the connection of the pore and throat channels. Figure 3 shows the pore throat structure of a typical porous medium, as well as the oil and water distribution at different locations.  $\theta$  is the three-phase contact angle of oil, water and a solid wall, and  $\beta$  is the opening angle of the pore. When the oil–water interface is in the throat channel, the direction of the capillary force (pointing to the concave side of the liquid surface) is the same as the direction of the oil–water movement under water-wet conditions, and the capillary force is a type of driving force, as shown in Figure 3a. When the water flows out of the throat channel, the angle between the oil–water interface and the pore wall after equilibrium is  $\theta$ . When  $\theta + \beta > \pi/2$ , the oil–water two-phase interface will be reversed, at which time the capillary force will point to the water side and impede the movement of the oil–water front. That is, affected by the pore structure, even under water-wet conditions, the capillary force formed between the oil–water interface and the pore wall may become resistance under certain conditions.

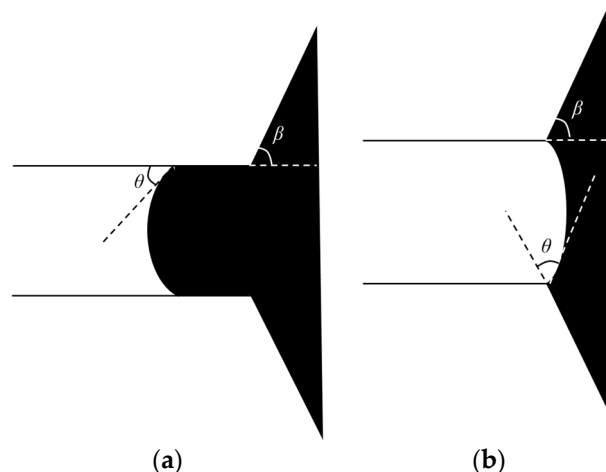


**Figure 3.** Oil and water distribution at different locations: (a) interface at the throat channel; (b) interface at the outlet section.

Figure 4 shows the morphology of the oil–water interface at different locations, and the capillary forces at the corresponding locations. In Figure 4,  $a-h$  indicates the morphology of the oil–water interface, and A–D is the position of the contact line. In the process of the water’s movement from the throat to the pore space, the oil–water interface undergoes three processes.

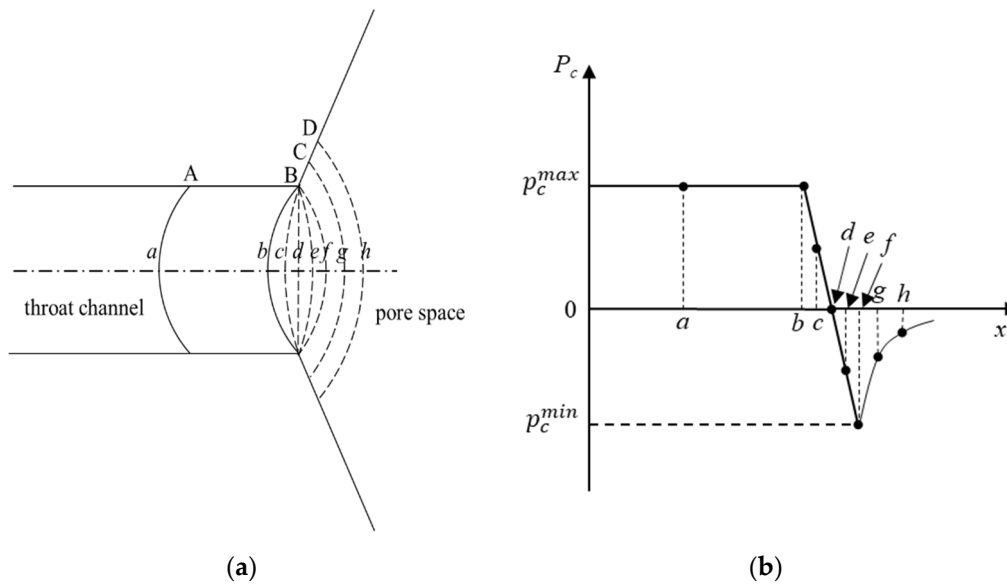


**Figure 4.** Schematic diagram of the oil–water interface morphology and capillary force variation along the axis: (a) the oil–water interface morphology at different locations; (b) the capillary force at different locations.

- (1) The oil–water interface advances in the throat channel (A→B); the morphology of the oil–water interface is shown as *a* or *b*. At this stage, the capillary force is a kind of driving force, and its value is given as

$$p_c^{max} = \frac{\sigma \cos(\theta)}{R}, \quad (21)$$

- (2) After the oil–water interface advances to the B position, the oil–water interface only deforms without moving forward (the three-phase contact line stays at B position) until the equilibrium wetting angle  $\theta$  between the interface of deformation and the water-side pore wall is reached (the oil–water morphology is shown as *b*). In this process, the capillary force formed on the wall of the oil–water pore first changes from  $p_c^{max}$  to 0 (the interface morphology is shown as *d*); after that, the oil–water interface reverses and the capillary force becomes negative until the negative extreme value of  $p_c^{min}$  is reached.

$$p_c^{min} = \frac{\sigma \cos(\min(\theta + \beta, \pi))}{R}, \quad (22)$$

- (3) Thereafter, the contact line moves further forward (B→D), the equivalent radius of the channel gradually increases, and the capillary force gradually decreases, at which time the morphology of the oil–water interface is shown in position *g* and *h*. The change of the capillary force in this stage is shown in Figure 4b (*f*→*h*).

As shown in Figure 4, when  $\theta + \beta > \pi/2$ , the oil–water interface reverses during the advancing process, the capillary force presents resistance under water-wet conditions, and there is a negative maximum value of  $p_c^{min}$ . When the driving force of the fluid is insufficient to overcome this maximum resistance, the oil–water interface will stop advancing, and increasing and decreasing the driving force in this process will only lead to the deformation of the interface. When the driving force of the fluid can overcome the maximum resistance, the value of the resistance will decrease, and the oil–water interface will still advance even at a low driving pressure. Therefore, the driving pressure must be above a certain threshold to induce fluid motion, and once this threshold value is reached, the displacement force required for fluid motion will decrease. For the sake of discussion, conveniently, the phenomenon is called the capillary barrier, and this threshold value is

named capillary barrier pressure. When the driving force exceeds the opening pressure of the capillary barrier pressure, the channel will be opened, and the fluid can move with little driving pressure; when the driving force is lower than the opening pressure of the capillary barrier pressure, the channel will be blocked by the capillary force, the fluid cannot move in the channel, and the fluid becomes stagnant.

The motion behavior of oil–water at the pore-scale can be determined by the relative magnitude of the viscous force and capillary force, and the viscosity ratio of oil–water [15]. The relative magnitude of viscous force and capillary force can generally be expressed by the capillary number:

$$Ca = \frac{u\mu_w}{\sigma}, \quad (23)$$

where  $u$  is the velocity of the fluid,  $\mu_w$  is the viscosity of the fluid, and  $\sigma$  is the interfacial tension coefficient. The comparison of the motion characteristics of oil and water under different capillary number can generally be realized by changing one of the three variables in the above equation.

#### 4. Physical and Numerical Conditions

##### 4.1. Physical Model

The core was sampled from the Chang 2 stratum, Xing 5009 well at the Xingzichuan Oil Production Plant in the Yanchang Oilfield, at a depth of 896 m. The stratum is a light gray oil-bearing fine sandstone. The sampled core was scanned via CT technology, and the obtained images were segmented to obtain the pore structure image of the core shown in Figure 5. The gray parts in the figure are pore channels. The pore size distribution is shown in Figure 6.

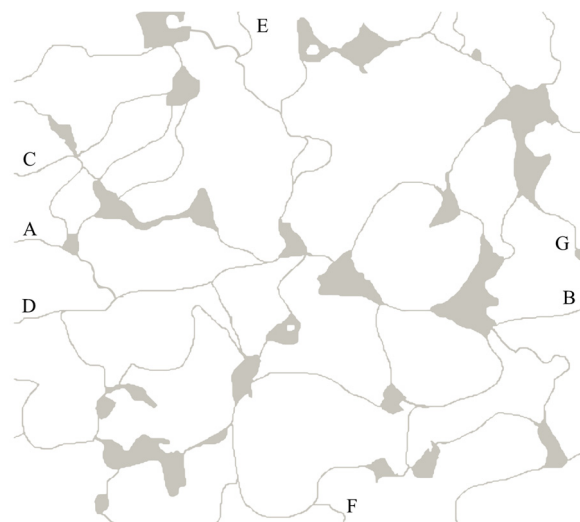


**Figure 5.** The pore structure of the core. A–G represent the inlet or outlet at different cases.

##### 4.2. Numerical Boundary Conditions

The numerical boundary conditions are given in Table 1. The Dirichlet boundary condition was employed for the velocity at the inlet and the wall, the pressure at the outlet, and the water volume fraction at the inlet. The Neumann boundary condition was employed for the velocity at the outlet, the pressure at the inlet and the wall, and the water volume fraction at the outlet. The constant contact angle boundary condition was used for the water–oil–solid contact line on the wall. The Gamma Scheme presented in work [29] was used to discretize the convection term, and the Crank–Nicolson scheme was for the time term [30]. The residual errors of the different physical quantities were set to  $10^{-6}$ . The Courant number in the simulation was set to 0.1, and the time step was adjusted adaptively [6].

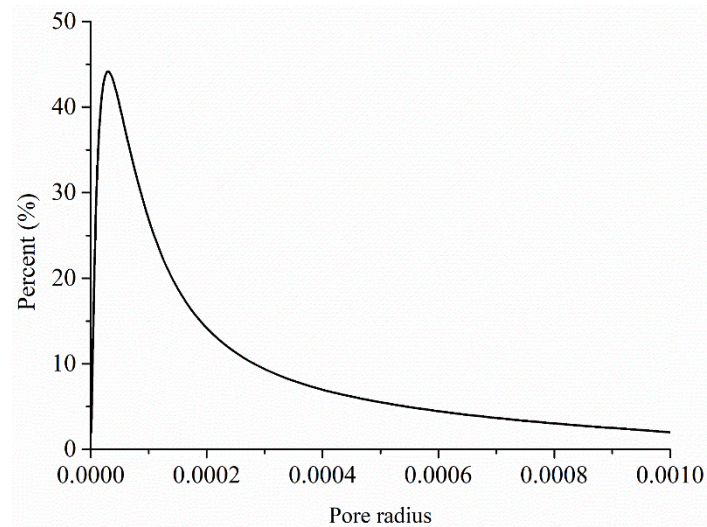


Figure 6. Pore size distribution.

Table 1. Numerical boundary conditions.

Physical Quantity	Boundaries		
	Inlet	Outlet	Wall
velocity	fixed value	zero gradient	no slip
pressure	zero gradient	fixed value	zero gradient
water volume fraction	fixed value	zero gradient	Constant contact angle

## 5. Results and Discussion

### 5.1. Oil–Water Two-Phase Flow Characteristics under Different Water Injection Rates

The physical model used for the simulation is shown in Figure 5, where A is the inlet; B is the outlet; C, D, E, F and G are closed and set as walls; and the other boundaries are walls. The pore space of the core is filled with oil at the initial moment, and then water is injected into the pore space at  $0.005 \text{ m}\cdot\text{s}^{-1}$ ,  $0.01 \text{ m}\cdot\text{s}^{-1}$ ,  $0.015 \text{ m}\cdot\text{s}^{-1}$ ,  $0.02 \text{ m}\cdot\text{s}^{-1}$ , and  $0.025 \text{ m}\cdot\text{s}^{-1}$  from inlet A, respectively. The viscosity ratio of oil to water is 10, the wetting angle is  $45^\circ$  (under this wettability condition, the capillary may show resistance or driving force, and the displacement process with this contact includes more extensive flow behaviors), and the tension coefficient at the oil–water interface is  $0.07 \text{ kg}\cdot\text{m}^{-2}$ .

Figure 7 shows the variation of the final oil recovery rate with the injection rate under continuous water injection conditions. It can be seen from Figure 7 that the highest recovery is achieved when the injection rate is  $0.01 \text{ m}\cdot\text{s}^{-1}$ . The capillary number  $Ca$  is  $2.14 \times 10^{-4}$ . Both too-low and too-high injection velocities fail to achieve the highest oil recovery rate. In order to clarify the underlying reason behind this phenomenon, in-depth analyses of the flow characteristics of the oil and water phases in the pore space at three injection rates of  $0.005 \text{ m}\cdot\text{s}^{-1}$  ( $Ca = 7.14 \times 10^{-5}$ ),  $0.01 \text{ m}\cdot\text{s}^{-1}$  ( $Ca = 1.43 \times 10^{-4}$ ) and  $0.03 \text{ m}\cdot\text{s}^{-1}$  ( $Ca = 4.29 \times 10^{-4}$ ) were conducted, respectively.

Figure 8 demonstrates the spatial distribution of oil and water at different times at an injection velocity of  $0.005 \text{ m}\cdot\text{s}^{-1}$  ( $Ca = 7.14 \times 10^{-5}$ ). As shown in the figure,  $a-n$  are the positions in the pore structure where capillary barriers may occur when the oil–water interface moves to these locations. Table 2 shows the occurring time of capillary barriers at these locations, the time of restart, the blockage duration, and the blockage ratio (the ratio of blockage time to total displacement time). The oil and water distribution at  $0.75 \text{ s}$  are shown in Figure 8a, and the oil–water interface moves to position  $a$ , as shown in the figure. This position is at the junction of the throat and the pore. When the oil and water move to this position, the capillary barrier phenomenon will be observed. When the driving pressure is insufficient, the capillary barrier will prevent the oil–water interface

from further movement, thus leading to the stagnation of the oil–water interface. As can be seen from Table 2, the capillary pressure barrier pressure here was not overcome until the end of the displacement process. As the displacement proceeds, the oil–water interface is prevented from advancing at position *b* at 0.97 s, and the oil–water movement stops. At this time, the oil–water interface in the upstream channel at position *c* was still advancing until 1.15 s when the oil–water interface was blocked at position *c*. The blockage at position *c* caused the pressure at the inlet to rise, thus restarting the original blockage at the oil–water interface at position *b*. At this time, the distribution of oil and water is shown in Figure 8b. Then, the oil and water continue to move until 1.31 s and the oil–water interface moves to position *d*, where the blockage occurs again. At this time, the oil–water interface in the upstream channels at positions *e* and *f* is still moving; the oil–water interface is blocked at position *e* at 1.41 s (as shown in Figure 8c), and the oil–water interface in the upstream channels at *f* moves rapidly, and is blocked at position *f* at 1.53 s. The motion of the fluid in all of the channels is blocked by the capillary barrier, resulting in a rise in the upstream pressure; the capillary barrier at position *d* is overcome, and the oil–water interface is restarted at 1.53 s. When the oil–water interface enters the pore after passing through position *d*, the oil–water interface is concave to the water side influenced by the pore structure, showing a resistance state. The increase of the upstream pressure results in the overcoming of the capillary barrier pressure at position *e* at 1.75 s. After the breakthrough, the oil and water distribution at 1.92 s are shown in Figure 8d. Then, the oil and water move further downwards after a brief blockage at 2.81 s at position *g*, and move to the lower right outlet of position *g*. Although the channel on the upper side of *g* is perpendicular to the displacement direction and the oil–water interface enters the smaller channels, the oil and water can still flow upward by imbibition under the low displacement speed. The final oil and water distribution are shown in Figure 8f.

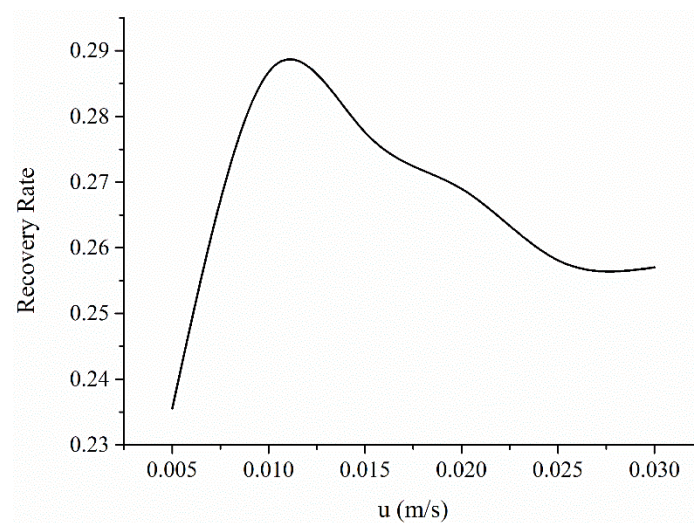


**Figure 7.** Variation of the final oil recovery rate with the injection velocity.

From the abovementioned oil–water flow process, we can find that the capillary barrier has a significant effect on the oil–water flow dynamics under the low capillary number. When the capillary pressure barrier is formed, the oil–water interface will block the channel where it is located, resulting in a change of the pressure transmission path in space and prompting the fluid flow to divert. When the capillary barrier is formed in the main displacement direction—for example, at position *b* or *d*—the capillary barrier will prevent the oil–water front from advancing, thus causing lateral sweeping. In this case, the capillary barrier formed at position *b* will cause the fluid to advance rapidly in the upstream channel of position *c*. When the capillary barrier is formed at position *d*, the velocity of the fluid will accelerate in the upstream channel of position *e* and the upstream channel of position *f*. When the capillary barrier is formed in the lateral direction, the

stagnant oil–water interface will prevent the further advancing of the oil and water flow, thus resulting in the formation of residual oil. For instance, the formation of capillary barriers at positions *a* and *c* prevented the further movement of oil and water, resulting in the formation of residual oil on the upper right side of positions *a* and *c*.

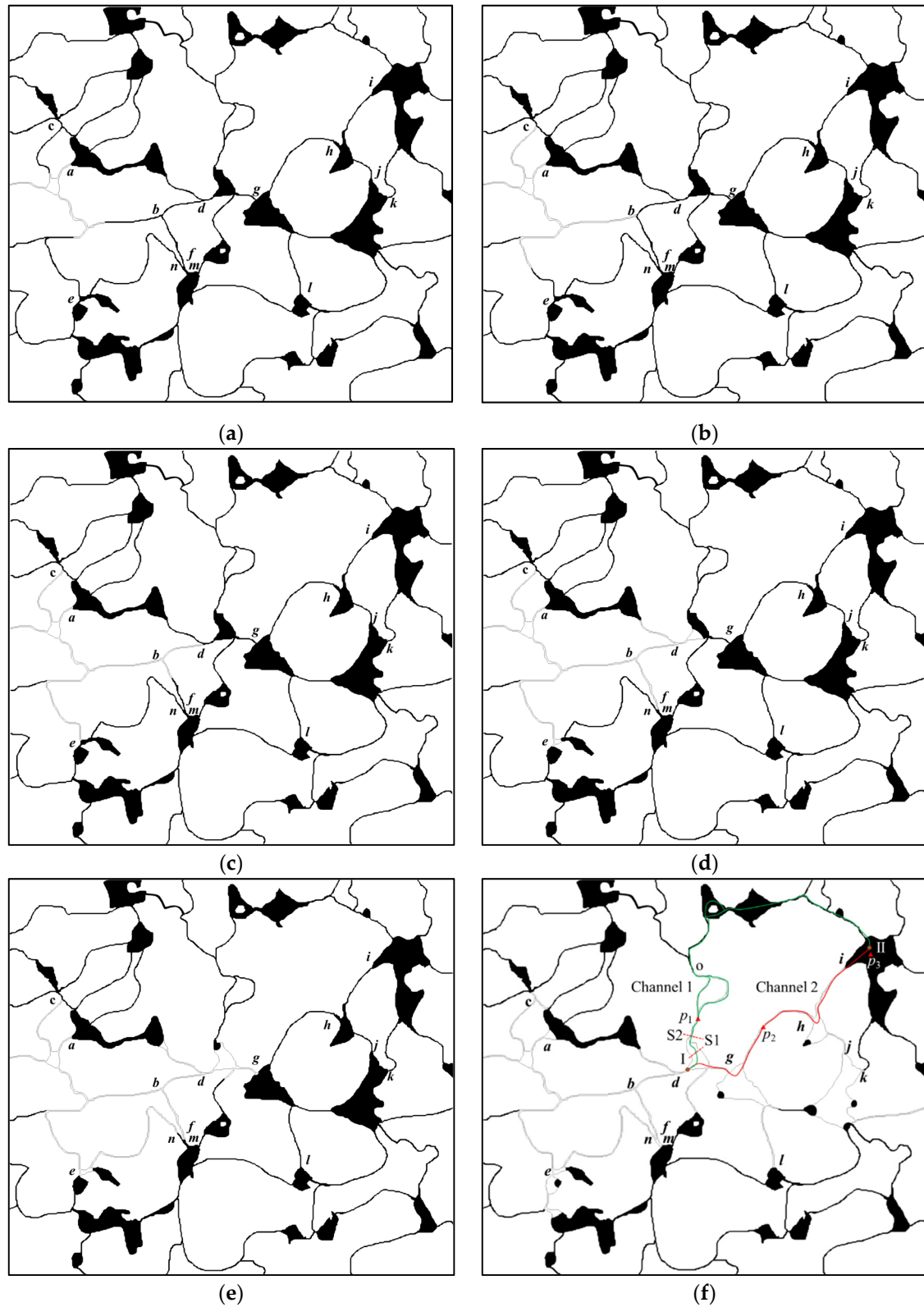


**Figure 8.** Oil and water distribution at different times, at the injection velocity of  $0.005 \text{ m}\cdot\text{s}^{-1}$  ( $\text{Ca} = 7.14 \times 10^{-5}$ ): (a) 0.75 s, (b) 1.15 s, (c) 1.41 s, (d) 1.92 s, (e) 3 s, (f) final. Different positions are indicated by lower case letters.

**Table 2.** Blocking and restart information at different positions during the injection process, at the injection velocity of  $0.005 \text{ m}\cdot\text{s}^{-1}$  ( $\text{Ca} = 7.14 \times 10^{-5}$ ).

Position	Blockage Time(s)	Restart Time(s)	Blockage Duration(s)	Blocking Ratio
<i>a</i>	0.750	$\infty$	$\infty$	$\infty$
<i>b</i>	0.970	1.150	0.180	0.0193
<i>c</i>	1.150	$\infty$	$\infty$	$\infty$
<i>d</i>	1.310	1.530	0.220	0.0236
<i>e</i>	1.410	1.750	0.340	0.0364
<i>f</i>	1.530	3.120	1.590	0.1704
<i>g</i>	2.810	2.880	0.070	0.0075
<i>h</i>	*	*	*	*
<i>i</i>	*	*	*	*
<i>j</i>	*	*	*	*
<i>k</i>	*	*	*	*
<i>l</i>	8.100	$\infty$	$\infty$	$\infty$
<i>m</i>	3.200	$\infty$	$\infty$	$\infty$
<i>n</i>	3.050	3.120	0.070	0.0075

$\infty$  The movement of the oil–water interface at this position has not been resumed at the end of the displacement process. \* The oil–water interface has not moved to this position.

Figure 9 shows the oil–water distribution at different times at the injection velocity of  $0.01 \text{ m}\cdot\text{s}^{-1}$  ( $\text{Ca} = 1.43 \times 10^{-4}$ ). Also, the blockage and restart information at different locations during the injection process is given in Table 3. The oil–water sweep process before the breakthrough of the capillary barrier at position *d* is almost the same as the oil–water sweep process at the injection velocity of  $0.005 \text{ m}\cdot\text{s}^{-1}$ . After the advancing of the oil–water interface through position *d*, the oil–water interface enters the pore space from the throat channels and presents a resistance state. Influenced by the capillary resistance at position *d*, the capillary barrier pressure at position *c* is overcome at 0.9 s. The oil–water interface advances further until a new capillary barrier appears. Due to the high injection velocity relative to the previous example, the oil–water interface advancing will not form an effective pressure barrier at position *g*, and it advances further forward through this position. The oil–water interface passing through position *g* first enters the channel between *g* and *h* and moves rapidly to position *h*. Position *h* is at the point from the throat to the pore space, and the oil–water interface presents a resistance state after passing through position *h* (as shown in Figure 9b). This resistance effect displaces the fluid to flow along the branch above the pore space in the middle of *dg*. After passing through the pore space downstream of position *h*, the oil–water interface moves further forward, and the capillary pressure barrier is formed at positions *i* and *j*. The blocking phenomenon observed at positions *i* and *j* promotes the transport of oil in the pore space below position *g* toward the outlet, as shown in Figure 9c. The blockage at position *j* is broken at 3.6 s. After the oil–water interface enters the pore space, a new oil–water interface is formed at position *k*, and this oil–water interface prevents the oil from flowing from the throat channel into the pore space. Meanwhile, the interface in the pore channel above the pore space between *d* and *g* stops advancing at position *o*.

It can be observed that there are differences in the sweep process and the final oil–water distribution at the two different injection velocities by comparing Figure 8 with Figure 9. As shown in Figure 8f, the sweep amount of channel 1 is more than that of channel 2 under low-velocity injection conditions; Figure 9d shows that the sweep amount of channel 1 is less than that of channel 2 under high-velocity injection conditions. This is largely due to the difference in the time of the oil–water interface entering the two channels, and an inhibition effect on the flow in the other channel is exerted by the oil–water interface entering the present channel.

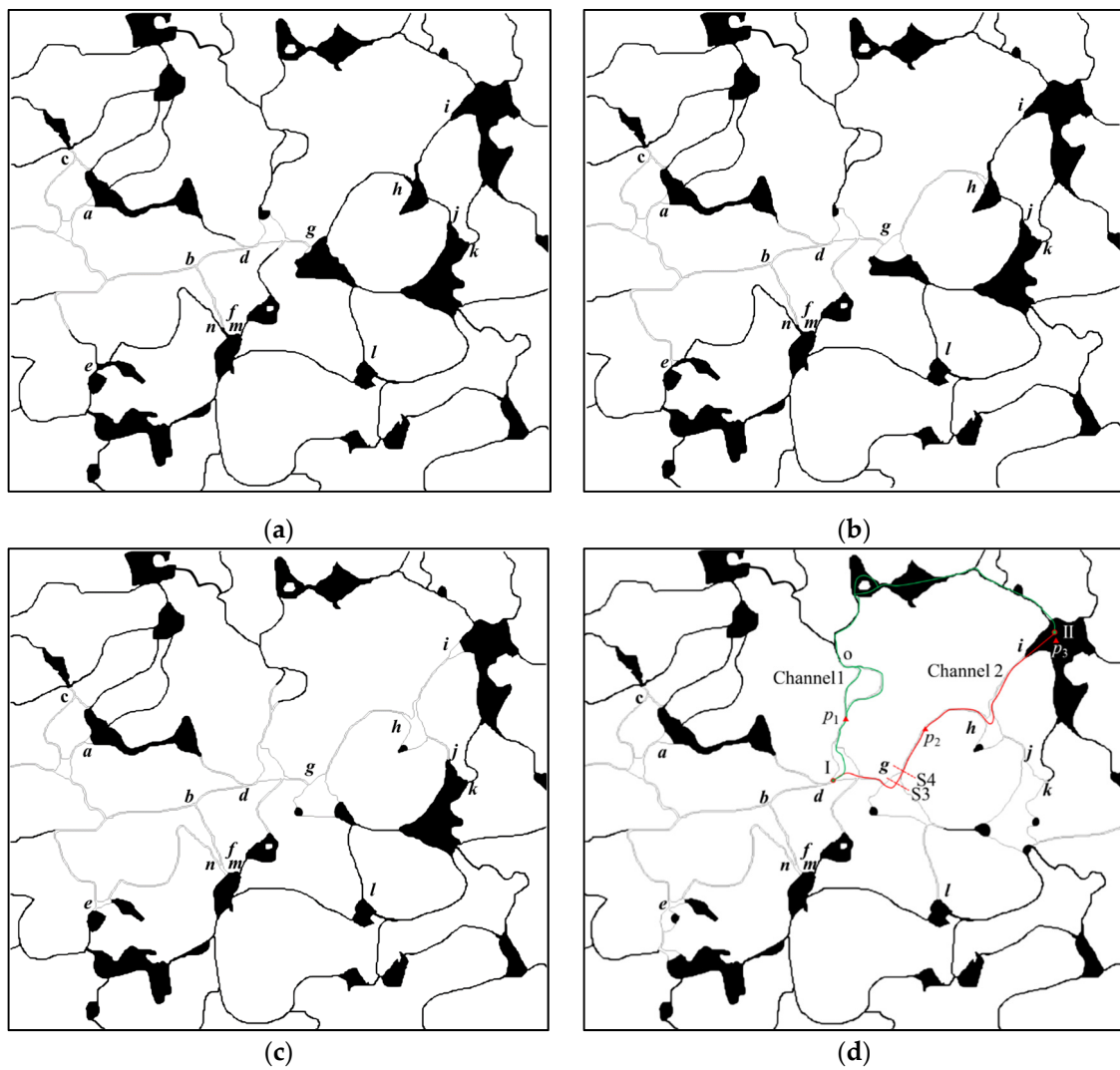


**Figure 9.** Oil and water distribution at different times, at the injection velocity of  $0.01 \text{ m}\cdot\text{s}^{-1}$  ( $\text{Ca} = 1.43 \times 10^{-4}$ ): (a) 1.2 s, (b) 1.9 s, (c) 3.3 s, (d) final. Different positions are indicated by lower case letters.

**Table 3.** Blockage and restart information at different locations during the injection process, at the injection velocity of  $0.01 \text{ m}\cdot\text{s}^{-1}$  ( $\text{Ca} = 1.43 \times 10^{-4}$ ).

Position	Blockage Time(s)	Start Time(s)	Blockage Duration(s)	Blockage Ratio
<i>a</i>	0.340	$\infty$	$\infty$	$\infty$
<i>b</i>	0.510	0.540	0.030	0.00528
<i>c</i>	0.540	0.900	0.360	0.0634
<i>d</i>	0.630	0.700	0.070	0.0123
<i>e</i>	1.820	1.970	0.150	0.0264
<i>f</i>	0.700	3.160	2.460	0.433
<i>g</i>	1.180	1.180	0	0
<i>h</i>	1.850	1.850	0	0
<i>i</i>	2.450	$\infty$	$\infty$	$\infty$
<i>j</i>	3.150	3.600	0.450	0.0792
<i>k</i>	4.260	$\infty$	$\infty$	$\infty$
<i>l</i>	5.490	$\infty$	$\infty$	$\infty$
<i>m</i>	3.280	$\infty$	$\infty$	$\infty$
<i>N</i>	3.160	3.160	0	0

$\infty$  The movement of the oil–water interface at this position has not been resumed at the end of the displacement process.

The aforementioned inhibition effect is illustrated in Figure 10. As shown in Figure 10, channel a and channel b are connected with channel c, respectively, and the fluid is driven from left to right. Water first flows into channel b, and an oil–water interface is formed in channel b. The oil–water interface in channel b changes the local pressure state, such that the pressure of the fluid pointed to the concave surface is higher than that of the other side. The pressure on the oil side in channel b is higher than the pressure on the water side under water-wet conditions, resulting in a higher pressure at point C, which reduces the pressure difference between the AC and inhibits the fluid flow in channel a. This is called the inhibiting effect of imbibition on flow in parallel channels.

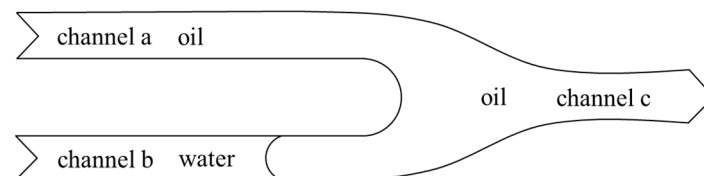


**Figure 10.** Schematic diagram of the capillary inhibition effect between the parallel channels. Different flow paths are distinguished by a–c.

In order to further illustrate the existence of the inhibition effect induced by the capillarity, the pressure changes at point  $p_1$ ,  $p_2$  and  $p_3$  in Figures 8f and 9d when the oil–water interface enters channel 1 or channel 2 were monitored. Table 4 shows the pressure at each point and the relevant pressure difference for the following four scenarios:

**Table 4.** Pressure at each point for different scenarios.

Pressure (Pa)	Scenario I	Scenario II	Scenario III	Scenario IV
$p_{p1}$	10,242.2	15,495.5	24,403.8	23,604.7
$p_{p2}$	6895.57	7199.75	22,444	24,639
$p_{p3}$	6876.09	7430.86	19,975.5	20,088.5
$p_{p1}-p_{p3}$	3366.11	8064.64	4428.3	3516.2
$p_{p2}-p_{p3}$	19.48	−231.11	2468.5	4550.5

Scenario I: the injection velocity is  $0.005 \text{ m}\cdot\text{s}^{-1}$ , water first enters channel 1 as shown in Figure 8f, and the oil–water interface moves to position S1 shown in Figure 8f.

Scenario II: the injection velocity is  $0.005 \text{ m}\cdot\text{s}^{-1}$ , water first enters channel 1 as shown in Figure 8f, and the oil–water interface moves to position S2 shown in Figure 8f.

Scenario III: the injection velocity is  $0.01 \text{ m}\cdot\text{s}^{-1}$ , water first enters channel 2 as shown in Figure 9d, and the oil–water interface moves to position S3 shown in Figure 9d.

Scenario IV: the injection velocity is  $0.01 \text{ m}\cdot\text{s}^{-1}$ , the water first enters the channel 2 shown in Figure 9d, and the oil–water interface moves to position S4 shown in Figure 9d.

It can be seen from Table 4 that the extent of the pressure increase at point  $p_1$  is much greater than that at point  $p_2$  when the water first flows into channel 1. The pressure difference in channel 1 increases greatly, while the pressure difference of the fluid in channel 2 reduces significantly. That is, the flow in channel 2 connected in parallel with channel 1 is inhibited to a large extent after the formation of the oil–water interface in channel 1. The pressure at point  $p_1$  decreases, while the pressure at points  $p_2$  and  $p_3$  increases when the water first flows into channel 2. The pressure difference in channel 2 increases, while the pressure difference in channel 1 decreases. That is, the flow of fluid in channel 1, which is connected in parallel with channel 2, is inhibited after the formation of the oil–water interface in channel 2. When the displacement force of the fluid is not sufficient to overcome the inhibiting effect of the capillarity, the oil–water two-phase flow stops, or a backflow (reverse imbibition) phenomenon is observed, thus reducing the oil recovery rate. Therefore, the inhibiting effect is stronger than the driving effect at an ultra-low injection velocity, which results in a relatively lower oil recovery rate.

A schematic conceptual model of two parallel channels—as shown in Figure 11—was

constructed in this paper to further analyze the disturbing effect of capillary forces on the flow in parallel channels from the quantitative perspective.

$$q_1 = \frac{R_2}{R_1 + R_2}q - \frac{p_{c2}}{R_1 + R_2} + \frac{p_{c1}}{R_1 + R_2}, \quad (24)$$

$$q_2 = \frac{R_1}{R_1 + R_2}q - \frac{p_{c1}}{R_1 + R_2} + \frac{p_{c2}}{R_1 + R_2}, \quad (25)$$

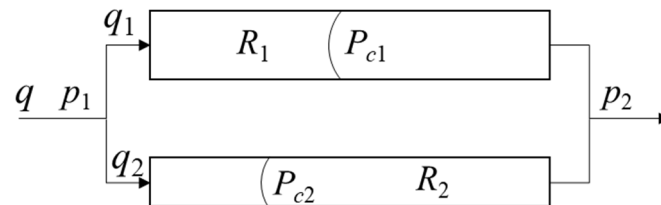


**Figure 11.** Schematic diagram of the parallel channels.

Figure 11 shows the schematic diagram of two parallel channels. As shown in Figure 11,  $q$  is the total flow rate of the two channels;  $q_1$  and  $q_2$  are the flow rates of channel 1 and channel 2, respectively;  $R_1$  and  $R_2$  are the viscous resistance of the two channels; and  $P_{c1}$  and  $P_{c2}$  are the capillary forces induced by the oil–water interface formed in the channels. The average flow rates of each channel expressed in Equations (24) and (25) are obtained by analyzing the flow in two parallel channels. It can be seen from the equations that the oil–water interface formed in a capillary tube will have an effect on the flow in its parallel channels. For instance, the capillary force induced by the formed oil–water interface in the channel (the capillary pressure is denoted as  $P_{c1}$ ) will facilitate the increase of the fluid flow rate in channel 1 and the decrease of the fluid flow rate in channel 2. A similar effect is observed at the oil–water interface formed in channel 2. To summarize, the capillary force induced by the oil–water interface formed in a channel acting as a kind of driving force will inevitably impede the two-phase flow in its parallel channel, and vice versa. The magnitude of the impeding and promoting effect is closely related to the ratio of the capillary force to viscous resistance, and the ratio is the distributing amount between parallel-connected channels.

The oil and water distribution at different times at the injection velocity of  $0.03 \text{ m}\cdot\text{s}^{-1}$  is shown in Figure 12. The capillary barrier may be formed along the path  $a-n$ , and the occurring time of the capillary barriers at these locations, the time of restart, the blockage duration, and the blockage ratio are shown in Table 5. As shown in Table 5, a persistent blockage is formed at positions  $a$  and  $m$ , while a transient blockages are observed at positions  $f$  and  $n$ . Blockage phenomena are not observed at other locations. The water phase advances along the direction of the main displacement under the pressure of the fluid, and a new oil–water interface is formed continuously. The newly formed oil–water interface will impede the lateral oil–water movement, which is referred to as the capillary blockage effect.

The blockage effect of the capillary force is illustrated in Figure 13. The displacement direction is from left to right, and the water first breaks through along channel b and channel c at the initial stage. A new oil–water interface is formed in channel a when the oil–water interface passes through position c. The capillary force induced by the oil–water interface under water-wet conditions will impede the further advancing of oil in channel a. This effect will result in the surplus of the oil in the lateral direction.

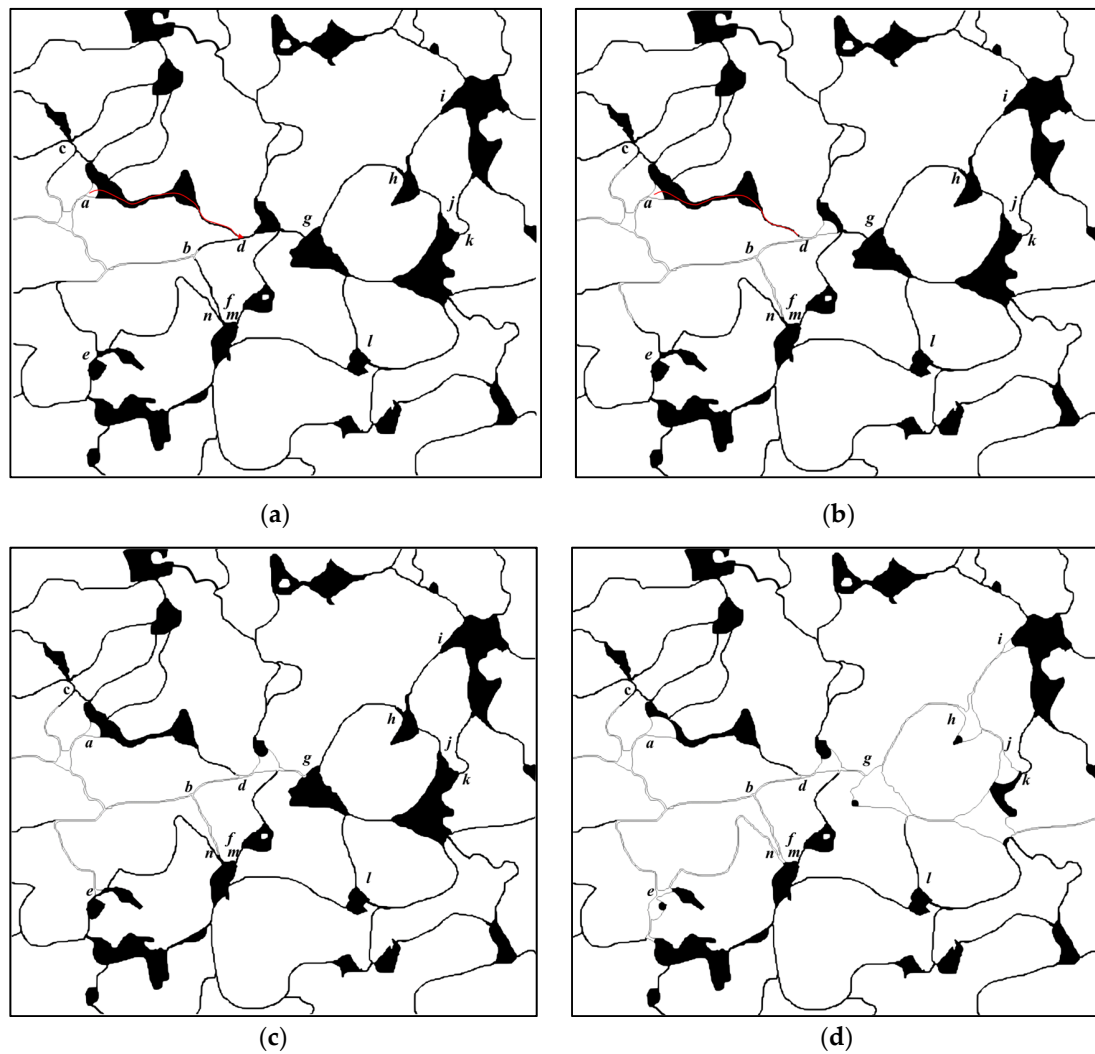


**Figure 12.** Oil and water distribution at different times, at the injection velocity of  $0.03 \text{ m}\cdot\text{s}^{-1}$  ( $\text{Ca} = 4.29 \times 10^{-4}$ ): (a) 0.19 s, (b) 0.31 s, (c) 0.39 s, (d) final. Different positions are indicated by lower case letters.

**Table 5.** Blockage and restart information at different locations during the injection process, at the injection velocity of  $0.03 \text{ m}\cdot\text{s}^{-1}$  ( $\text{Ca} = 4.29 \times 10^{-4}$ ).

Position	Blockage Time(s)	Restart Time(s)	Blockage Duration(s)	Blockage Ratio
<i>a</i>	0.210	$\infty$	$\infty$	$\infty$
<i>b</i>	0.185	0.185	0	0
<i>c</i>	*	*	*	*
<i>d</i>	0.220	0.220	0	0
<i>e</i>	0.360	0.360	0	0
<i>f</i>	0.290	1.300	1.010	0.5940
<i>g</i>	0.390	0.390	0	0
<i>h</i>	0.700	0.700	0	0
<i>i</i>	0.980	0.980	0	0
<i>j</i>	1.100	1.100	0	0
<i>k</i>	*	*	*	*
<i>l</i>	*	*	*	*
<i>m</i>	1.350	$\infty$	$\infty$	$\infty$
<i>n</i>	1.150	1.300	0.150	0.0882

$\infty$  The movement of the oil–water interface at this position has not been resumed at the end of the displacement process. \* The oil–water interface has not moved to this position.

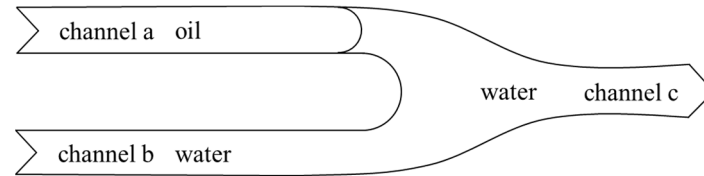
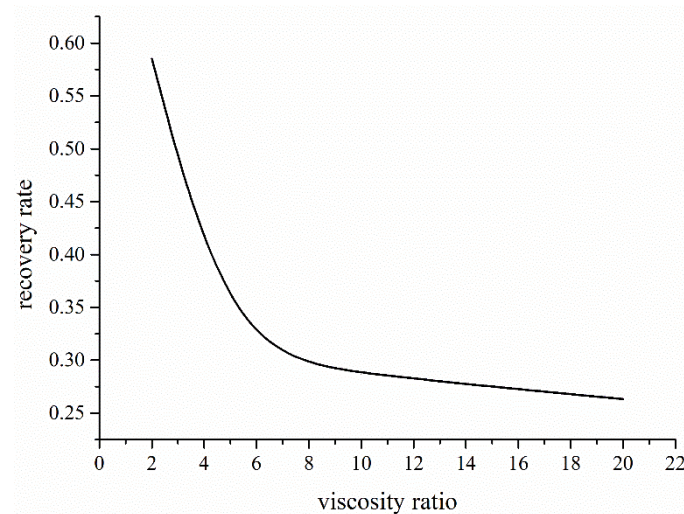


**Figure 13.** Schematic diagram of the blocking effect in the capillary tube. Different flow paths are distinguished by a–c.

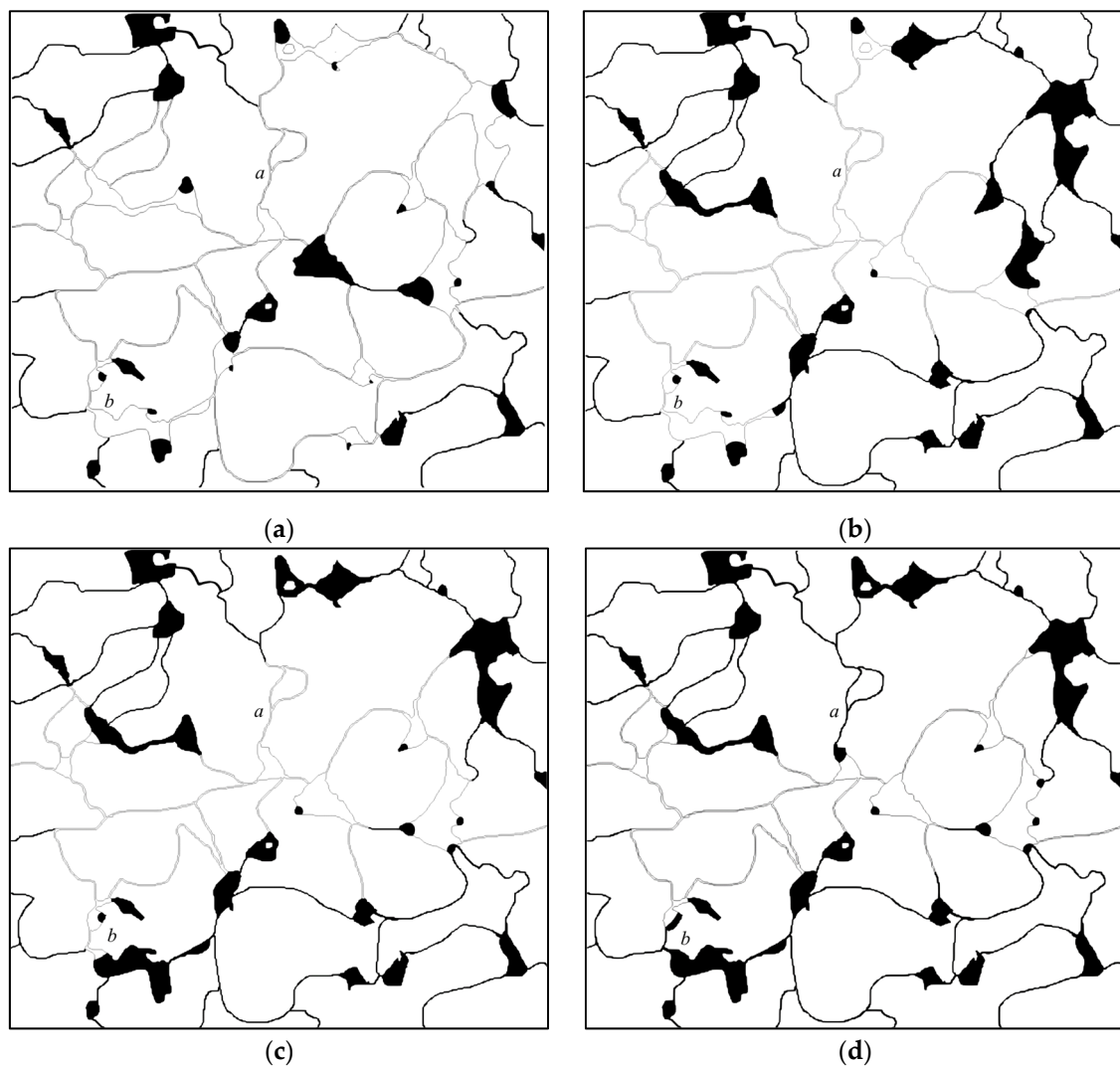
As shown in Figure 12a, the oil in the pore space downstream of position *a* can enter the main channel through the *a–d* channel (colored in red) and flow downstream before the oil–water interface reaches position *d*. Once the water flows past position *d*, an oil–water interface will be formed at one end of position *d* in the *a–d* channel. The formed oil–water interface will impede the movement of oil and water in the *a–d* channel, which will reduce its movement speed or block the channel. A larger distance needs to be bypassed before the oil in the pore space downstream of position *a* enters the main channel, which reduces the speed of the oil movement in the lateral channel. The lateral blockage effect gradually becomes stronger as new oil–water interfaces continue to form downstream, and the distance the oil needs to bypass is greater, eventually causing the oil to fail to flow into the main channel from the lateral direction, which results in a great deal of residual oil being trapped in the pore space. Therefore, the faster the injection rate, the quicker the occurrence of the blocking effect induced by the newly formed oil–water interface. The failure of the oil in the lateral direction to enter the main channel in a timely manner will lead to the lower oil recovery rate. Too high an injection rate will facilitate the rapid formation of water-bearing channels in the main displacement direction, and will reduce the oil recovery rate.

### 5.2. Oil–Water Two-Phase Flow Characteristics under Different Viscosity Ratios

The variation of the final oil recovery rate with the oil–water viscosity ratio at an injection rate of  $0.01 \text{ m}\cdot\text{s}^{-1}$  ( $\text{Ca} = 1.43 \times 10^{-4}$ ) is shown in Figure 14. The water viscosity is set to a fixed value of  $10^{-3} \text{ kg}\cdot\text{m}^{-1}\cdot\text{s}^{-1}$  in each simulation process, while the oil viscosity is constantly changing. It can be seen from Figure 15 that the oil recovery rate decreases with the increase of the oil–water viscosity ratio when the viscosity ratio is less than 7, while the increase of the viscosity ratio has little impact on the oil recovery rate when the viscosity ratio is greater than 7.



**Figure 14.** Variation of the final oil recovery rate with the oil–water viscosity ratios.



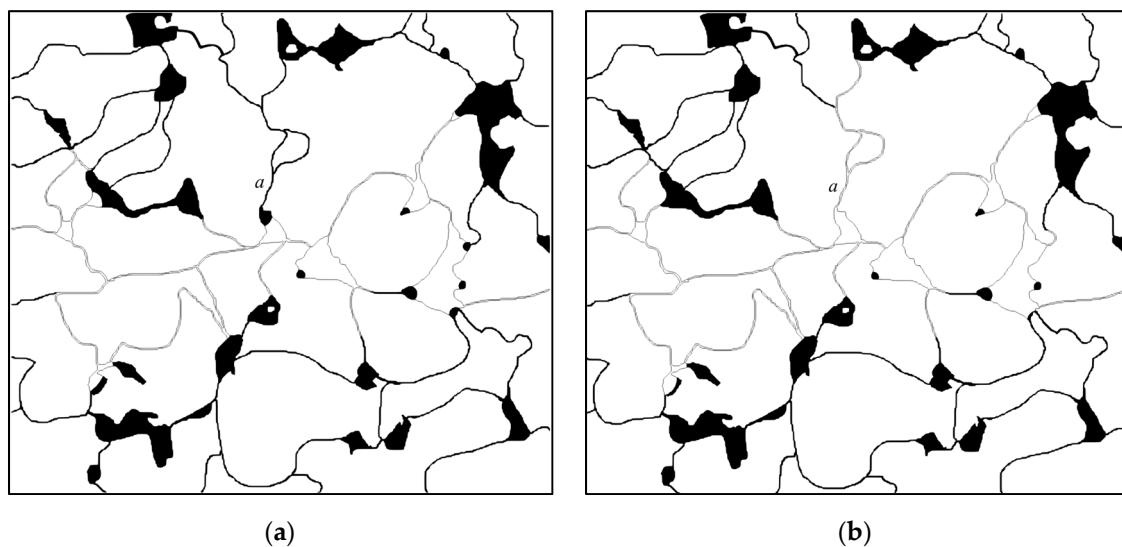
**Figure 15.** The final oil and water distribution at an injection rate of  $0.01 \text{ m}\cdot\text{s}^{-1}$  with different viscosity ratios: (a) at the oil–water viscosity ratio of 2; (b) at the oil–water viscosity ratio of 5; (c) at the oil–water viscosity ratio of 10; (d) at the oil–water viscosity ratio of 20. Different positions are indicated by lower case letters.

Figure 15 shows the final oil and water distribution at an injection rate of  $0.01 \text{ m}\cdot\text{s}^{-1}$  ( $\text{Ca} = 1.43 \times 10^{-4}$ ) with different oil–water viscosity ratios. It can be seen from Figure 15a that the sweep space of water flooding is larger when the oil–water viscosity ratio is small. Multiple paths are formed from the inlet to the outlet, resulting in a higher final oil recovery rate. The degree of sweep of the water flooding on both sides of the main channel gradually decreases with the increase of the oil–water viscosity ratio (as shown in Figure 15b–d). The degree of sweep of the water flooding in channel *a* and channel *b* gradually decreases with the increase of the oil–water viscosity ratio.

This change is due to the dynamic inhomogeneity induced by the change of phase distribution during the displacement process, and the dynamic inhomogeneity can be elucidated using the parallel-connected channels shown in Figure 11. The capillary barrier effect is not taken into account in the parallel-connected channels, i.e.,  $P_{c1} = 0$  and  $P_{c2} = 0$ . Besides this, assuming that  $R_1 < R_2$ , according to Equations (24) and (25), the volumetric flow rate in channel 1 is greater than that in channel 2. The oil in the two parallel channels is gradually displaced by water, and the average viscosity of the fluid in the channels decreases as water advances within the two channels. The flow rate in channel 1 is greater and the resistance of the channel decreases faster than that of channel 2, thus further increasing the flow rate of channel 1. The velocity of the fluid advancing in the channel is

higher than that of channel 2, which leads to the viscous fingering in the channel. The larger the oil–water viscosity ratio, the stronger the dynamic inhomogeneity as the displacement process proceeds. Meanwhile, the phenomenon of viscous fingering is more obvious and the degree of sweep of the displacement is lower.

It can be known from Equations (24) and (25) that the flow rate of the two channels is influenced by the viscosity of oil and water, and the capillary effect. The effect of capillarity on the volumetric flow rate of the branch channels is closely related to the ratio of the capillary force to the sum of viscous resistance  $R_1 + R_2$  of the two channels. As the displacement process proceeds, the oil in channel 1 and channel 2 is gradually displaced by water,  $R_1$  and  $R_2$  decrease, and the effect of capillarity on the distribution of the volumetric flow rate gradually intensifies. Providing that the oil–water viscosity ratio stays constant in all cases, the capillary effect plays a significant role in the oil displacement process when the absolute value of the viscosity is lower. Figure 16 shows the final oil and water distribution at different absolute viscosities, with a viscosity ratio of 20 at an injection rate of  $0.01 \text{ m}\cdot\text{s}^{-1}$  ( $\text{Ca} = 1.43 \times 10^{-4}$ ). In this case, the oil–water viscosity ratio is the same, while the absolute viscosity is different. It can be seen from the figure that the oil in channel *a* is not displaced when the absolute oil–water viscosity is larger, and vice versa. Therefore, under the premise of the same oil–water viscosity ratio, the smaller the absolute viscosity of oil and water, the greater the role of the capillary effect in the flow. The capillary fingering is easier to form, and the lateral displacement of oil will be observed.



**Figure 16.** The final oil and water distribution at different absolute viscosities, with a viscosity ratio of 20: (a) the effective viscosity of water is  $0.001 \text{ kg}\cdot\text{m}^{-1}\cdot\text{s}^{-1}$  and oil is  $0.02 \text{ kg}\cdot\text{m}^{-1}\cdot\text{s}^{-1}$ ; (b) the effective viscosity of water is  $5 \times 10^{-4} \text{ kg}\cdot\text{m}^{-1}\cdot\text{s}^{-1}$  and oil is  $0.01 \text{ kg}\cdot\text{m}^{-1}\cdot\text{s}^{-1}$ . Different positions are indicated by lower case letters.

### 5.3. Characteristics of the Oil–Water Flow under Different Adjustment Strategies

The adjustment of the injection direction, turning the oil well to the injection well, and increasing the water injection rate are important measures in the process of oil recovery, and are adopted after the initial water flooding. The spatial distribution of the oil and water is more complex compared with that of the pre-water flooding period. The numerical simulation of water flooding process was conducted using the physical model of the core shown in Figure 5 in order to create a more complex residual oil distribution before the pre-adjustment. Ports A, C and D are injection ports; port G is the outlet; and ports B, E and F are closed and set as walls. The injection velocity is  $5 \times 10^{-3} \text{ m}\cdot\text{s}^{-1}$  ( $\text{Ca} = 7.14 \times 10^{-5}$ ), the viscosity of oil is  $0.02 \text{ kg}\cdot\text{m}^{-1}\cdot\text{s}^{-1}$ , the viscosity of water is  $0.001 \text{ kg}\cdot\text{m}^{-1}\cdot\text{s}^{-1}$ , and the oil–water interfacial tension is  $0.07 \text{ kg}\cdot\text{m}^{-2}$ . The final distribution of the residual oil is shown in Figure 17 after continuous water flooding until no oil is displaced from the outlet.

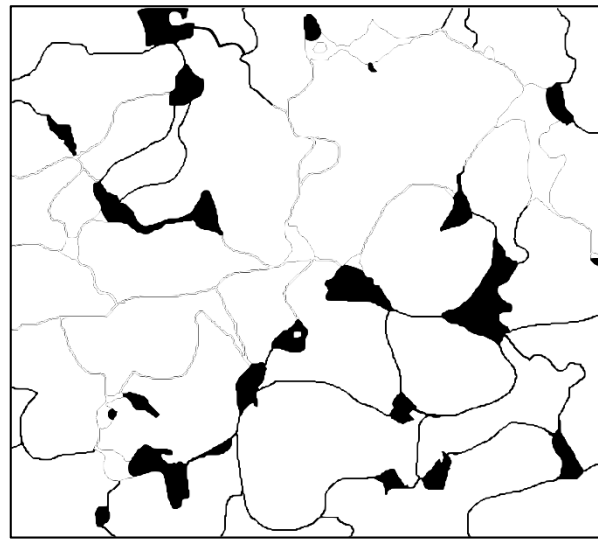


Figure 17. Oil and water distribution before adjustment.

### 5.3.1. Adjustment of the Injection and Extraction Direction

The oil and water distribution at different times after adjusting the injection and extraction direction (injection from port E and outflow from port F at an injection rate of  $5 \times 10^{-3} \text{ m}\cdot\text{s}^{-1}$ ) are shown in Figure 18. A water-bearing channel is formed in the core after continuous water flooding before adjustment, and the remaining oil is observed in the upper and lower parts of the porous structure. There exists a capillary barrier at positions *a*, *b*, *c*, *d*, and *e* where the oil–water interface is stagnant. The displacement pressure is insufficient to overcome the capillary force induced by the capillary barrier and the oil–water interface stops advancing, which results in the remaining of oil in the pore space. The remaining oil on the upper side of the water-bearing channel moves downward under the pressure of displacement after the adjustment of the injection and extraction direction. As shown in Figure 18a, the oil in position *h* moves downward under the displacement pressure, and is split into two streams of fluid—*f* and *g*—at the bifurcation of the pore channel. The capillary force in channel *h* is a kind of driving force (oil displaced by water) due to the water-wet characteristic of the pore structure, while the capillary force (water displaced by oil) induced by the two-phase interface in channels *f* and *g* is a kind of resistance. The capillary force is relatively strong under low-velocity injection conditions, and the capillary resistance in channels *f* and *g* determines the distribution of the volumetric flow rate in the two channels. The final distribution of the volumetric flow rate in channels *f* and *g* is almost identical due to the similar radius of the two pore channels, as shown Figure 18b. As the displacement process proceeds, the flow stream in channel *f* is further divided into two streams along channels *f*<sub>1</sub> and *f*<sub>2</sub>, respectively, and the amount of oil distributed in each channel is similar, as shown in Figure 18c. The oil distributed in channel *f*<sub>2</sub> is eventually displaced downstream, forming oil droplets in the pore space adhering to the pore wall (as shown in Figure 18d). Although there is a pressure difference upstream and downstream of channel *f*<sub>1</sub>, as shown in Figure 18d, the magnitude of the capillary force at two ends of the remaining oil is different, and the difference of the capillary forces at two ends of the remaining oil balances the pressure difference between the two ends of the oil column, which leads to the remaining of the oil.

For the fluid below the water-bearing channel, the capillary barriers formed at positions *a*, *b*, *c*, *d*, and *e* have an inhibiting effect on the fluid flow (as shown in Figure 18a), while the capillary force is a kind of driving force at position *i* when the oil–water interface advances within the throat channel. Therefore, the interface at position *i* moves first in the displacement process (comparing the changes of Figure 18c with Figure 18b). The decrease of the capillary force at the interface of position *i* leads to increase of the displacement pressure upstream when water moves to the pore body. The oil–water interface at positions

*a*, *b*, *c*, *d*, and *e* resumes moving (as shown in Figure 18c). The channels where the interfaces at position *a* and position *i* are formed have low resistance, and the volumetric flow rate of each channel is larger. Eventually, two new oil–water interfaces at positions *a*<sub>1</sub> and *a*<sub>2</sub> are formed when the fluid flows downstream from the pore space at position *a* and then flows out of channel F. The capillary forces induced by the two newly formed interfaces will impede the movement of oil and water under water-wet conditions, causing the oil in the lower right corner to reach an equilibrium state.

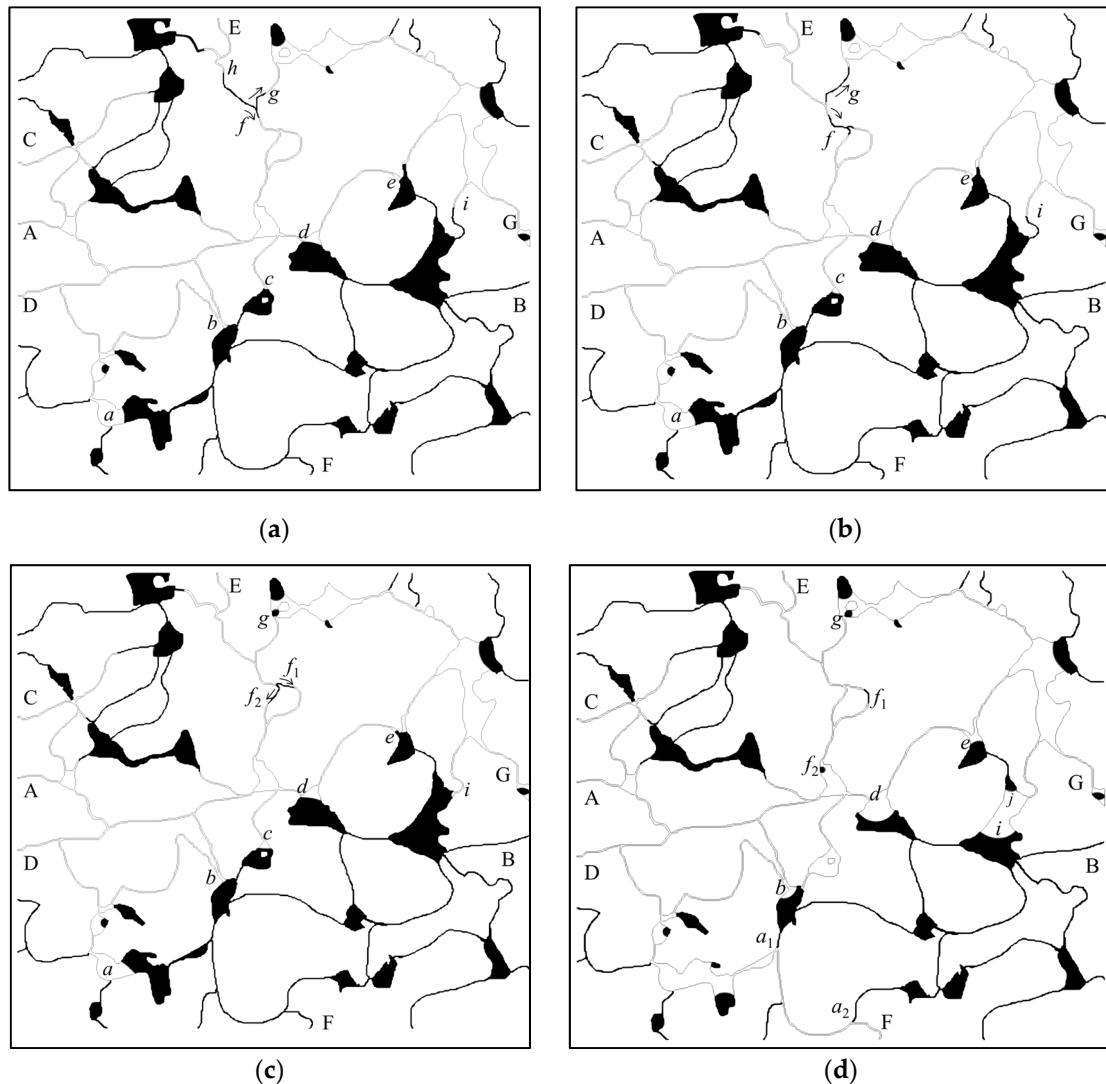


**Figure 18.** Changes of oil and water distribution after adjusting the injection and extraction direction: (a) 0.05 s after adjustment; (b) 0.1 s after adjustment, (c) 0.15 s, and (d) final. Different positions are indicated by lower case letters.

### 5.3.2. Turning the Extraction Well to the Injection Well

A water-bearing channel was formed between ports A and G in the pre-water-flooding process. No oil will be displaced from port G if water is continuously injected at the same rate. Turning the extraction-well to the injection-well method can be used to further improve the oil recovery rate. Figure 19 shows the oil and water distribution and flow path during the pre-displacement and post-displacement period, at an injection rate of  $0.005 \text{ m}\cdot\text{s}^{-1}$ . Water is injected from ports A and G, and F is the outlet. As shown in Figure 19, the light blue overlay area and light red overlay area are the control regions of injection port A and injection port G, respectively. The cyan line is the flow path of fluid

flowing from port A, and the red line is the flow path of fluid flowing from port B. Points *a–n* are the intersection points of the flow paths.

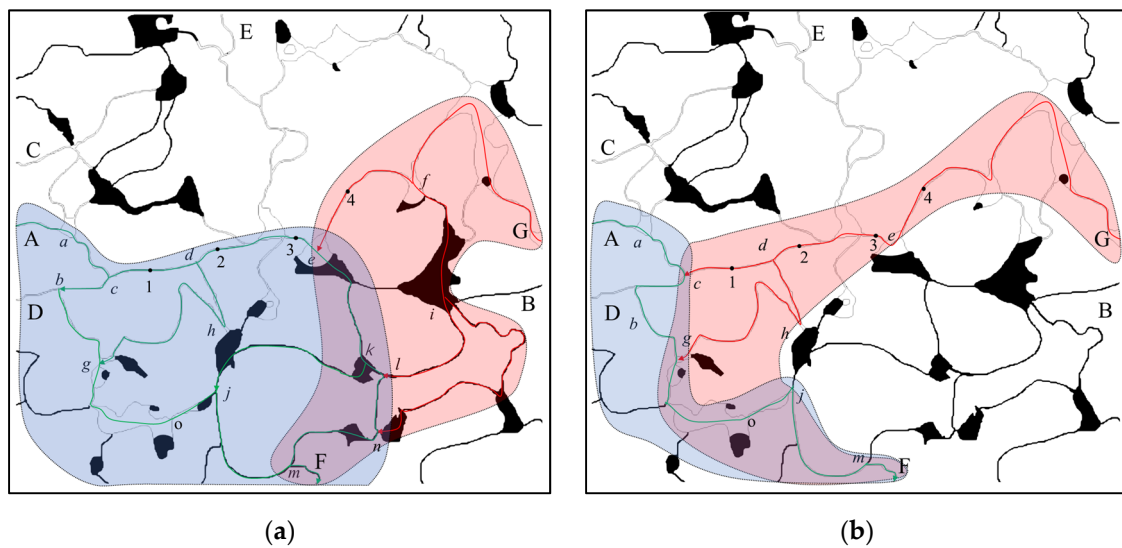


**Figure 19.** Flow paths and the residual oil distribution in different periods under simultaneous continuous injection conditions at port A and port G: (a) oil and water distribution during the pre-displacement, (b) final residual oil distribution.

Figure 19a shows the oil and water distribution in the mobilization process of the remaining oil during the pre-displacement. It can be seen from the figure that the control area of port A is much larger than that of injection port G. The fluid in port A plays a significant role in the mobilization of the oil in the channel along the path *bgjmF*, as well as the oil in the channel along path *eklnmF* and the channel along path *ekjmF*. The oil gradually flows out through outlet F as the displacement process proceeds, and the remaining oil in the channel along the path *bgjmF* is gradually displaced by water. A new oil–water interface is formed when the water front advances through the intersection point *j*. The remaining oil flowing through the *kj* channel to the *jm* channel will be prevented from moving by the newly formed oil–water interface. The movement of the oil in the *kj* channel will stop when the upstream displacement pressure is insufficient to overcome the resistance. The newly formed oil–water interface will prevent the migration of oil in channel *nm* to channel *mF* when the water front advances through the intersection point *m*. The final residual oil distribution and the flowing path is shown in Figure 19b.

In order to further clarify the change of the flowing path in the displacement process, flow velocities at the four selected points (points 1–4) shown in the figure were monitored. The velocity variation with time at these four points is shown in Figure 20. The velocity value is positive if the fluid flows from left to right, and the velocity value is negative if the fluid flows from right to left. It can be seen from the figure that the velocity of each point has been changing as the injection process proceeds. Small-scale fluctuations appeared in the local region, and dramatic changes of the velocity with time were observed. In addition, the velocity of points 1, 2, and 3 is reversed between 1 s and 1.5 s.

In order to account for the aforementioned velocity reversal, the forces exerted on the two-phase fluid within the pore space were analyzed in detail. The fluid flow within the pore space mainly resulted from the viscous action and the capillarity:

- (1) Viscous action: The viscous action allows the fluid to flow at a more uniform velocity, and the viscosity will not purely cause large velocity fluctuations during the flow process. The viscous effect determines the magnitude of the volumetric flow rate in different channels when there is no oil–water interface formed. For instance, the volumetric flow rate of channels along the paths *iln* and *in* at intersection point *i* are different at the initial displacement stage.

- (2) Capillarity: (a) The magnitude of the capillary force is influenced by the size of the pore channel, and changes with the positions of the oil–water interface, thus causing the acceleration or deceleration of the fluid in local regions. As shown in Figure 20, the velocity of point 2 at time I fluctuates dramatically (flow reversal), which is mainly due to the abrupt decrease of the pore channel when the oil–water interface moves to position *o*, as shown in Figure 19. When the fluid flows from the pore space to the throat channels, the capillary force will accelerate the flow rate of the local fluid, which is a type of driving force, resulting in the velocity decrease of point 2 first, and then the velocity acceleration of point 2 in the reverse direction. (b) Influenced by the abrupt change of the pore channel and the wettability conditions of the wall, the capillary force may show resistance or driving force characteristics. The oil–water interface stops moving if the displacement pressure is insufficient to overcome the capillary resistance, prompting the flow path to change. As shown in Figure 20 at time II (1.12 s), the large velocity fluctuations of point 2 and the velocity reversal of point 3 can be observed. The oil–water interface stops moving when the displacement pressure is insufficient to overcome the capillary resistance induced by the newly formed interface at position *j*, and the original flow path *kj* is blocked, resulting in the reversal of the flow path *ed*. Therefore, the main reason for the fluid reversal at points 1, 2, and 3 is the capillary blockage effect.

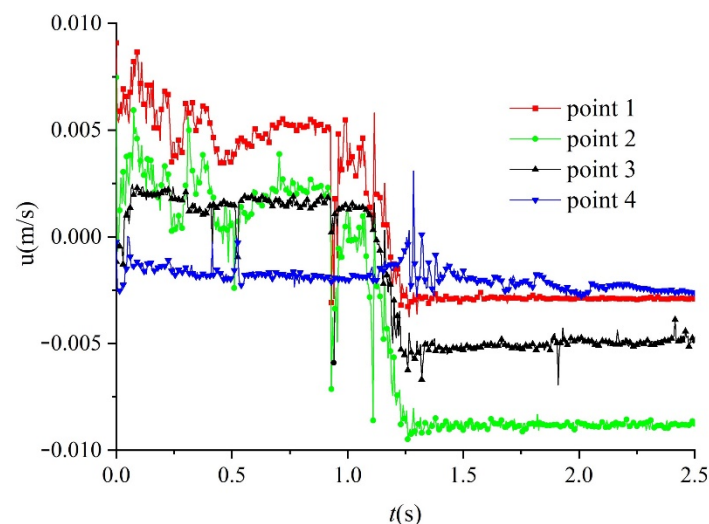


**Figure 20.** Velocity variation of different detection points with time.

Figure 21 shows the variation of the inlet pressure and the oil saturation of the core with time. It can be seen from Figure 21a that the oil saturation of the core gradually decreases with time, and the oil saturation of the core is hardly changed after 1.25 s. The pressure at the left and right injection points almost remains constant before the formation of the oil–water interface at the intersection *j* (1.12 s) when injecting water from the left and right points simultaneously, and the oil saturation in the core remains almost constant with time during this period. The pressure variation is significantly different from that under single-point injection conditions. The pressure difference at the inlet and outlet gradually decreases with the decrease of the oil saturation in the core under single-point injection conditions due to the lower viscosity of water compared with that of oil. The precondition of the drawn conclusion is that the channels dominated by the injection port almost remain unchanged. However, the system has the effect of stabilizing the pressure when high water-bearing channels are formed between the two ports by injecting water into the core from the two ports, and the process of stabilizing the pressure is achieved by adjusting the flowing paths.

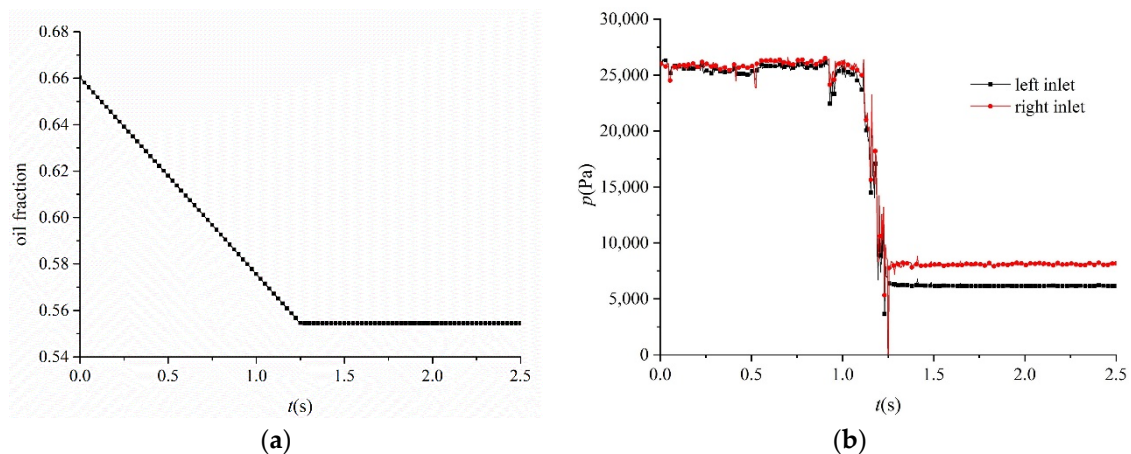


**Figure 21.** Variation of the inlet pressure and oil saturation with time: (a) oil saturation in the core sample with time; (b) pressure at the injection port with time.

### 5.3.3. Increasing the Water Injection Rate

Figure 22a shows the distribution and flow paths of the final residual oil after increasing the injection velocities. The black color in the figure is the remaining oil, and the red, light blue and cyan colors are the flow paths. Water is injected into the pore space at a rate of  $0.005 \text{ m/s}$  from ports A, D and C, and flows out from port G. As shown in the figure, there are clusters of residual oil in area I and II, and the rest of the residual oil is trapped in dead-end pore space. For the remaining oil in area I, the interfaces of the oil and water are located at positions  $a, b, c, d$  and  $e$ , respectively. Positions  $a, b$ , and  $c$  are located upstream, and  $d$  and  $e$  are located downstream. The capillary barrier formed due to the abrupt change of the pore radius at positions  $a, b$ , and  $c$  impede the further movement of the oil–water interface. The oil–water interface has an inhibiting effect on the movement of the oil–water two-phase flow when the oil–water interface at positions  $d$  and  $e$  move downstream (water displaced by oil).  $a', b', c', d'$ , and  $e'$  are points on the flow path connected to the channel where points  $a, b, c, d$ , and  $e$  are located, respectively. There is no movement of water in channels  $a'a, b'b, c'c, d'd$  or  $e'e$  due to the barrier effect of the oil–water interface, and due to there being no pressure drop in the channels. The oil and water movement will stop if the displacement pressure on the flow path is insufficient to overcome the capillary barrier pressure and the resistance of the water displacement by the oil. For instance, the oil in the channel between points  $a$  and  $e$  will not be mobilized when the pressure difference between points  $a'$  and  $e'$  is insufficient to overcome the capillary resistance (water displaced by oil) formed at points  $a$  and  $e$ . The dual resistance effect of the capillary barrier (point  $a$ ) and the capillary blockage effect (point  $e$ ) is the main reason for the formation of residual oil under water-wet conditions. Under water flooding conditions, increasing the volumetric flow rate of channels can mobilize the oil in channels  $a-e$ . The oil will flow if the pressure difference between points  $a'$  and  $e'$  on the flow path is sufficient to overcome the capillary resistance formed at points  $a$  and  $e$ . The formation process of residual oil in region II is similar to the formation process of residual oil in region I.

Figure 22b shows the final residual oil distribution after water flooding at an injection rate of  $0.005 \text{ m}\cdot\text{s}^{-1}$  (as shown in Figure 22a) with  $0.01 \text{ m}\cdot\text{s}^{-1}$  liquid extraction. From the perspective of the distribution and flow path characteristics, the mobilization effect of the residual oil is not obvious, and no flowing path is formed. It can be known from the oil–water interface position that interface  $f$  moves forward a little. Accordingly, interface  $l$  slightly moves forward along the elongated throat channel. Finally, the oil–water interface reaches a new equilibrium and the oil stops moving. The relationship between the injection rate and the mobilized amount of the remaining oil used is not always linear. Only when the injection rate reaches a certain threshold value and the pressure difference formed at the

different oil–water interfaces of the same remaining oil is higher than the dual resistance of the capillary barrier and capillary blockage, will the oil be mobilized.

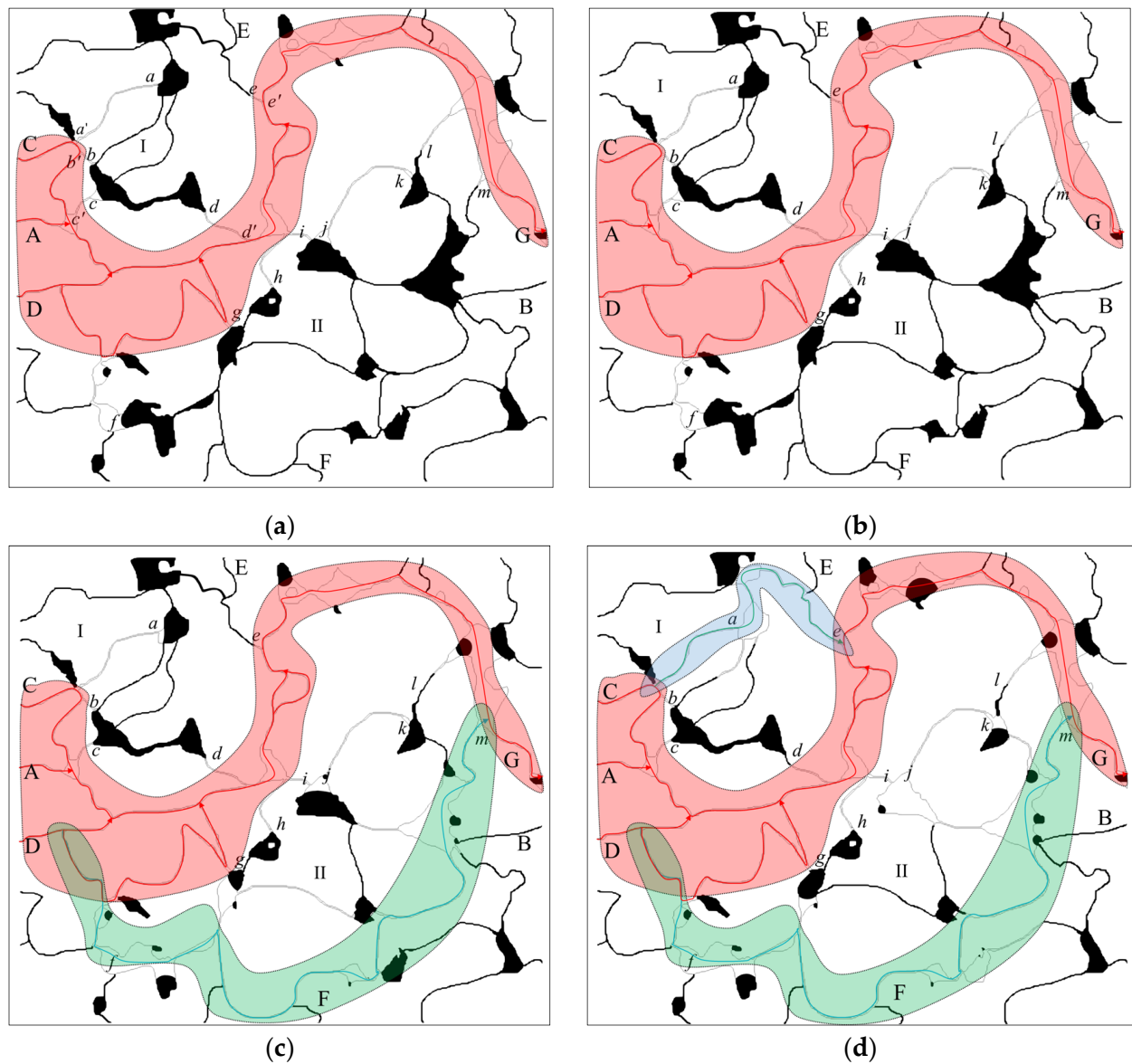


**Figure 22.** Final residual oil distribution and flow path characteristics after increasing the water injection rate: (a) residual oil after water flooding, at an injection velocity of  $0.005 \text{ m}\cdot\text{s}^{-1}$ ; (b) final residual oil at injection velocity of  $0.01 \text{ m}\cdot\text{s}^{-1}$  based on the results at a velocity of  $0.005 \text{ m}\cdot\text{s}^{-1}$ ; (c) final residual oil at an injection velocity of  $0.015 \text{ m}\cdot\text{s}^{-1}$  based on the results at a velocity of  $0.005 \text{ m}\cdot\text{s}^{-1}$ ; (d) final residual oil at injection velocity of  $0.02 \text{ m}\cdot\text{s}^{-1}$  based on the results at a velocity of  $0.005 \text{ m}\cdot\text{s}^{-1}$ . Different positions are indicated by lower case letters.

Figure 22c,d shows the residual oil at injection rates of  $0.015 \text{ m}\cdot\text{s}^{-1}$  and  $0.02 \text{ m}\cdot\text{s}^{-1}$  after the initial water injection at the rate of  $0.005 \text{ m}\cdot\text{s}^{-1}$ , respectively. The remaining oil is mobilized to some extent, and new flow paths are formed when increasing the injection rate of the water. For instance, the residual oil in region II is mobilized and a new flow path is formed (light blue) at the injection rate of  $0.015 \text{ m}\cdot\text{s}^{-1}$ , while the residual oil in region I and II is mobilized and two new flowing paths are formed (cyan and light blue) when the injection rate is increased to  $0.02 \text{ m}\cdot\text{s}^{-1}$ . Once a flow channel fully filled with water is formed between the main inlet and the flow outlet, increasing the water injection rate is an important measure to improve the oil recovery rate.

## 6. Conclusions

In this paper, the water flooding process in low-permeability sandstone oil reservoirs was numerically simulated using a Navier–Stokes equation coupled with the VOF method in order to systematically investigate the effects of viscous action and capillarity on the oil–water two-phase flow dynamics of water flooding. By studying the oil–water two-phase flow dynamics under different injection rates, the viscosity ratios of oil to water, and different adjustment strategies after water flooding, the following conclusions can be drawn:

- (1) The larger the viscosity ratio is, the stronger the dynamic inhomogeneity will be as the displacement process proceeds, and the greater the difference in the distribution of volumetric flow rate in different channels, which will lead to the formation of a growing viscous fingering phenomenon, thus lowering the oil recovery rate. Under the same viscosity ratio, the absolute viscosity of the oil and water will also have an essential impact on the oil recovery rate by adjusting the relative value of viscous action and capillarity. The change of the dynamic inhomogeneity induced by the viscous effect is a process of gradual change, and does not cause abrupt changes of the fluid velocity in the pore space. In the case of unidirectional displacement, the flow path does not change, the oil with high viscosity is gradually replaced by the oil with low viscosity in the pore channels, and the pressure difference between the inlet and the outlet decreases continuously as the displacement process proceeds. The two-way displacement strategy promotes the fluid to flow along the vertical direction of the displacement. The control regions of the injection with two ports constantly change as the displacement proceeds, and thereby the process of stabilizing the pressure is achieved by adjusting the flow paths.
- (2) Pore-scale phenomena induced by the capillary effect have a crucial impact on the pore-scale flow dynamics. The capillary barrier in the main displacement direction causes the flow of the fluid in lateral direction, and the capillary barrier in the lateral direction will impede the further flow of the fluid. Reducing the angle between the displacement direction and the direction of the capillary barrier pressure induced by adjusting the displacement direction can further improve the sweep area of the displacement fluid. The capillary imbibition will accelerate the fluid in the channel, and has an inhibiting effect on the fluid in parallel channels. The capillary blocking effect induced by the newly formed interface at the pore intersections can result in the sudden change of the fluid flow in the pore space.

There is an optimal displacement velocity for a specific pore structure. The capillary barrier in the lateral direction is difficult to break through at too low a displacement velocity, and the inhibiting effect of channels with percolation on parallel channels will be intensified, which affects the final oil recovery rate. Too high a displacement velocity will prompt the rapid formation of a new oil–water interface, and will form blockage in the measurement channel, thus reducing the final oil recovery rate. The dual effect of the capillary barrier and capillary blockage is the direct cause of the residual oil formation, and the main reason that residual oil can be mobilized only under a certain dynamic condition. The production of the remaining oil can only be completed under certain power conditions. Increasing the injection rate step by step is an important measure to improve oil recovery.

**Author Contributions:** Conceptualization, J.S. and T.N.; methodology, M.X. and J.S.; investigation, M.X. and B.H.; writing—original draft preparation, T.N. and B.H.; writing—review and editing, L.W. and C.H. All authors have read and agreed to the published version of the manuscript.

**Funding:** This research was funded by the National Natural Science Foundation of China, grant number: 12072256; the Natural Science Basic Research Plan in Shaanxi Province of China, grant number: 2021JM-406; the Excellent Youth Foundation of SINOPEC (P20009); and the Key Research and Development Program of Shaanxi (Program No. 2021GXLH-Z-071).

**Institutional Review Board Statement:** Not applicable.

**Informed Consent Statement:** Not applicable.

**Data Availability Statement:** Some or all data, models, or code that support the findings of this study are available from the corresponding author.

**Conflicts of Interest:** The authors declare no conflict of interest.

## References

1. Chai, R.; Liu, Y.; He, Y.; Liu, Q.; Xue, L. Dynamic behaviors and mechanisms of fluid-fluid interaction in low salinity waterflooding of carbonate reservoirs. *J. Pet. Sci. Eng.* **2021**, 109256. [[CrossRef](#)]
2. Zallaghi, M.; Khaz'Ali, A.R. Experimental and modeling study of enhanced oil recovery from carbonate reservoirs with smart water and surfactant injection. *Fuel* **2021**, *304*, 121516. [[CrossRef](#)]
3. Su, J.; Wang, L.; Gu, Z.; Zhang, Y.; Chen, C. Advances in Pore-Scale Simulation of Oil Reservoirs. *Energies* **2018**, *11*, 1132. [[CrossRef](#)]
4. Chai, G.L.; Wang, L.; Gu, Z.L.; Yu, C.; Zhnag, Y.; Shu, Q.; Su, J. A consistent sharp interface fictitious domain method for moving boundary problems with arbitrarily polyhedral mesh. *Int. J. Numer. Methods Fluids* **2021**, *93*, 2065–2088. [[CrossRef](#)]
5. Su, J.; Chai, G.; Wang, L.; Yu, J.; Cao, W.; Gu, Z.; Chen, C.; Meng, W. Direct numerical simulation of particle pore-scale transport through three-dimensional porous media with arbitrarily polyhedral mesh. *Powder Technol.* **2020**, *367*, 576–596. [[CrossRef](#)]
6. Su, J.; Chai, G.; Wang, L.; Cao, W.; Yu, J.; Gu, Z.; Chen, C. Direct numerical simulation of pore scale particle-water-oil transport in porous media. *J. Pet. Sci. Eng.* **2019**, *180*, 159–175. [[CrossRef](#)]
7. Su, J.; Chai, G.; Wang, L.; Cao, W.; Gu, Z.; Chen, C.; Xu, X.Y. Pore-scale direct numerical simulation of particle transport in porous media. *Chem. Eng. Sci.* **2019**, *199*, 613–627. [[CrossRef](#)]
8. Lenormand, R.; Touboul, E.; Zarcone, C. Numerical models and experiments on immiscible displacements in porous media. *J. Fluid Mech.* **1988**, *189*, 165–187. [[CrossRef](#)]
9. Swpu, P. Review on chemical enhanced oil recovery using polymer flooding: Fundamentals, experimental and numerical simulation. *Petroleum* **2020**, *6*, 115–122.
10. Kamal, M.S.; Hussein, I.A.; Sultan, A.S. Review on Surfactant Flooding: Phase Behavior, Retention, IFT, and Field Applications. *Energy Fuels* **2017**, *31*, 7701–7720. [[CrossRef](#)]
11. Liu, X.; Wang, L.; Wang, J.; Su, J. Pore-Scale Simulation of Particle Flooding for Enhancing Oil Recovery. *Energies* **2021**, *14*, 2305. [[CrossRef](#)]
12. Homsy, G.M. Viscous fingering in porous media. *Annu. Rev. Fluid Mech.* **1987**, *19*, 271–311. [[CrossRef](#)]
13. Cottin, C.; Bodiguel, H.; Colin, A. Drainage in two-dimensional porous media: From capillary fingering to viscous flow. *Phys. Rev. E* **2010**, *82*, 046315. [[CrossRef](#)] [[PubMed](#)]
14. Tsuji, T.; Jiang, F.; Christensen, K. Characterization of immiscible fluid displacement processes with various capillary numbers and viscosity ratios in 3D natural sandstone. *Adv. Water Resour.* **2016**, *95*, 3–15. [[CrossRef](#)]
15. Hu, R.; Lan, T.; Wei, G.-J.; Chen, Y.-F. Phase diagram of quasi-static immiscible displacement in disordered porous media. *J. Fluid Mech.* **2019**, *875*, 448–475. [[CrossRef](#)]
16. Singh, K.; Jung, M.; Brinkmann, M.; Seemann, R. Capillary-Dominated Fluid Displacement in Porous Media. *Annu. Rev. Fluid Mech.* **2019**, *51*, 429–449. [[CrossRef](#)]
17. Yang, Y.; Cai, S.; Yao, J.; Zhong, J.; Zhang, K.; Song, W.; Zhang, L.; Sun, H.; Lisitsa, V. Pore-scale simulation of remaining oil distribution in 3D porous media affected by wettability and capillarity based on volume of fluid method. *Int. J. Multiph. Flow* **2021**, *143*, 103746. [[CrossRef](#)]
18. Guo, Y.; Zhang, L.; Zhu, G.; Yao, J.; Sun, H.; Song, W.; Yang, Y.; Zhao, J. A Pore-Scale Investigation of Residual Oil Distributions and Enhanced Oil Recovery Methods. *Energies* **2019**, *12*, 3732. [[CrossRef](#)]
19. Berg, S.; Ott, H.; Klapp, S.A.; Schwing, A.; Neiteler, R.; Brussee, N.; Makurat, A.; Leu, L.; Enzmann, F.; Schwarz, J.-O.; et al. Real-time 3D imaging of Haines jumps in porous media flow. *Proc. Natl. Acad. Sci. USA* **2013**, *110*, 3755–3759. [[CrossRef](#)]
20. Roof, J. Snap-off of oil droplets in water-wet pores. *Soc. Pet. Eng. J.* **1970**, *10*, 85–90. [[CrossRef](#)]
21. Li, Z.; Gu, Z.; Li, R.; Wang, C.; Chen, C.; Yu, C.; Zhang, Y.; Shu, Q.; Su, J. Investigation on droplet dynamic snap-off process in a short, abrupt constriction. *Chem. Eng. Sci.* **2021**, *235*, 116496. [[CrossRef](#)]
22. Cha, L.M.; Xie, C.Y.; Feng, Q.H.; Balhoff, M. Geometric criteria for the snap-off of a non-wetting droplet in pore-throat channels with rectangular cross-sections. *Water Resour. Res.* **2021**, *57*. [[CrossRef](#)]
23. Rabbani, H.S.; Zhao, B.; Juanes, R.; Shokri, N. Pore geometry control of apparent wetting in porous media. *Sci. Rep.* **2018**, *8*, 1–8. [[CrossRef](#)]
24. Ubbink, O. *Numerical Prediction of Two Fluid Systems with Sharp Interfaces*; University of London: London, UK, 1997.
25. Issa, R.I. Solution of the implicitly discretised fluid flow equations by operator-splitting. *J. Comput. Phys.* **1986**, *62*, 40–65. [[CrossRef](#)]
26. OpenCFD, OpenFOAM. Available online: [www.openfoam.com](http://www.openfoam.com) (accessed on 13 September 2021).
27. Wang, L.; Tian, W.-X.; Zhao, X.-Y.; Huang, C.-Q. Numerical simulation of the effects of canopy properties on airflow and pollutant dispersion in street canyons. *Indoor Built Environ.* **2021**. [[CrossRef](#)]

- 
28. Raeini, A.Q.; Blunt, M.J.; Bijeljic, B. Direct simulations of two-phase flow on micro-CT images of porous media and upscaling of pore-scale forces. *Adv. Water Resour.* **2014**, *74*, 116–126. [[CrossRef](#)]
  29. Jasak, H.; Weller, H.G.; Gosman, A.D. High resolution NVD differencing scheme for arbitrarily unstructured meshes. *Int. J. Numer. Methods Fluids* **1999**, *31*, 431–449. [[CrossRef](#)]
  30. Crank, J.; Phyllis, N. A practical method for numerical evaluation of solutions of partial differential equations of the heat-conduction type. *Math. Proc. Camb. Philos. Soc.* **1947**, *43*, 431–449. [[CrossRef](#)]